Hydraulic control characterization a modal Froude number

Hydraulic control mechanism is based on the theory of supercritical flows, which uses a parameter called the internal Froude number to characterize the hydraulic state of the flow. The Froude number is a dimensionless quantity that expresses, in this case, the ratio of the velocity of a fluid to the velocity of a linear internal wave on the interface. Some studies have adapted this internal Froude number to two layers Flow (Armi[35]) or three layer flow (Sannino *et al.*[36]). Precise characterization of hydraulic control in complex stratification case is still in progress (K. Winters and L. Armi[37]). In our study, to qualify hydraulic control state, a modal Froude number, F_n, is adopted: $F_n(x,t) = \frac{\max_z U(x,t)}{c_n}$. F_n varies in space and time and compares over a fluid column the maximum value of fluid velocity, U, to the theoretical mode celerity, c_n, calculated above the flat bottom i.e. at the maximum strait depth (h=H=0.2). However the choice of the value of mode celerity above the strait will be discussed. Indeed, in linear theory, hydraulic control is located above the strait so above a varying topography. The modal decomposition does not apply for a varying bottom. So in controversial cases, a comparison between a modal decomposition in shallow water (at the shallowest strait depth h=D) and a modal decomposition in deep water (above the flat bottom at the maximum strait depth, h=H=0,2m) is made. In such cases, a second modal Froude number interpolated for shallow water is used: $F_{n,D}(x,t) = \frac{\max_z U(x,t)}{c_{n,D}}$, $c_{n,D}$ is the mode celerity calculated at the shallowest strait depth so for a total depth of D.

The objective is to understand the mechanism of internal wave generation in a large range of strait configurations in order to locate more precisely the induced mixing. We perform a large range

of simulations from linear regimes to highly non linear regimes. A focus is made on non-linear processes and interactions between internal waves, tidal currents and topography. First, a linear regime is investigated to highlight internal wave generation mechanism in this three-layer fluid. Vertical mode internal wave structures are compared with analytical solutions to validate the numerical configuration. A particular interest is given to supercritical topography and generation of higher vertical modes (section 2). Then we will focus on hydraulic control state in non-linear regime and approach breaking, instabilities phenomenon and relationship with solitary waves (section 3). The last section focuses on local strait circulation associated to these internal waves regimes (section 4).

4. Control by topography in linear regimes

The first objective is to compare the numerical configuration in linear regimes with the theoretical linear modal decomposition of Gerkema and Zimmerman[34] (section 1.c.i)). For that, in this section, all of the simulations are characterized by:

-a weak tidal forcing characterizing a subcritical fluid ($\frac{U_{max}}{c_1} \ll 1$) and a nonlinearity parameter ε inferior to 0.018 (threshold limit of Dossmann *et al.*[9] for a linear regime)

- a topographic blocking parameter *B*=0.7 , feature of shallow strait

- A fat pycnocline ($\delta\rho^* = \frac{\delta\rho}{H} = 0.3$) , approaching a three layer stratification. In the bottom layers, the stratification tends to zero in such a way that the propagation condition of linear internal waves is no longer satisfied: $\gg N_b$. So, the pycnocline is the only region where internal wave can propagate hence it becomes the waveguide of internal waves. In such configurations, it may be assumed that there is no internal wave's secondary generation as described in Dossmann *et al.*[10].

We will consider two different cases: a subcritical ($\frac{\theta_p}{\gamma} > 1$) and a supercritical topography ($\frac{\theta_p}{\gamma} < 1$) regarding to the pycnocline stratification. A focus is made on energy splitting between vertical modes in both cases. All numerical and physical parameters are indicated in table 3.

		Linear Regime ε<<0.018		
		Subcritical Topography $\frac{\theta_{th}}{\gamma} > 1$	Supercritical Topography $\frac{\theta_{th}}{\gamma} < 1$	
		Sim0	**Sim1**	**Sim2**
initial conditions	h_ρ, h_0	0.07, 0.07		
	Δρ, δρ	60, 0.06		
	T, A	16, 0.006		
	λ_r	1.5	0.5	0.3
Regime parameters	B	0.7		
	θ_{th}/γ	1.36	0.47	0.29
	ε	0.0014	0.0042	0.007
	λ_1/λ_r	1.5	4.4	7.3
	λ_2/λ_r	0.5	1.5	2.5
	λ_3/λ_r	0.3	0.9	1.5
	λ_4/λ_r	0.2	0.6	1.05
Validation	$\frac{\theta_{Sim}}{\theta_{th}}$	1.05	1.04	1.05
	$\frac{c_{n_{Sim}}}{c_{n_{th}}}$	0.98	0.98	0.97
		1	1.02	0.98
		-	1.02	1 /0.98
	$\frac{\lambda_{n_{Sim}}}{\lambda_{n_{th}}}$	0.97	0.998	0.88
		1.04	0.99	0.98
		-	0.95	0.97/0.96

TABLE 3–Numerical and physical parameters for linear regime

4.1. Subcritical topography

A simulation, **Sim0**, with subcritical topography, is shown in Figure 2 (d) after 5.6 forcing periods (*t*=90s). The primary four plots (a,b,c) are vertical velocity analytical fields calculated according to the stratification profile (*Δρ, δρ,h$_\rho$,H*) and the forcing periodicity (*T*) based on vertical modes decomposition approach. As the topography is subcritical, an assumption is made that the amplitudes of the vertical modes are inversely proportional to the mode number ($a_n \propto 1/n$). In these configurations, the vertical stratification profile is not linear, so the internal wave structure is more complex. In particular, the wavenumber, k_n, is no more linearly proportional to the mode number, *n*, even if the wavenumber still grow with the mode number. Consequently, we assume that the amplitudes of the vertical modes are rather proportional to the wavenumber ($a_n \propto 1/k_n$).

The first plot (a) takes into account only the first vertical mode and in each following plot we superimposed one additional vertical mode so the third plot (c) finally shows the first three vertical modes. The bottom plot (d) represents the vertical velocity output from **Sim0** at t=5.6T. The main differences between theory (a,b,c) and the numerical experiment (d) are the representation of the generation area and the transition state. Indeed method of vertical modes rest on the assumption of a flat bottom and lead to a steady state solution. That's why in our study, vertical modes are characterized only above flat bottom and not in the strait area (above the ridge) where they are generated.

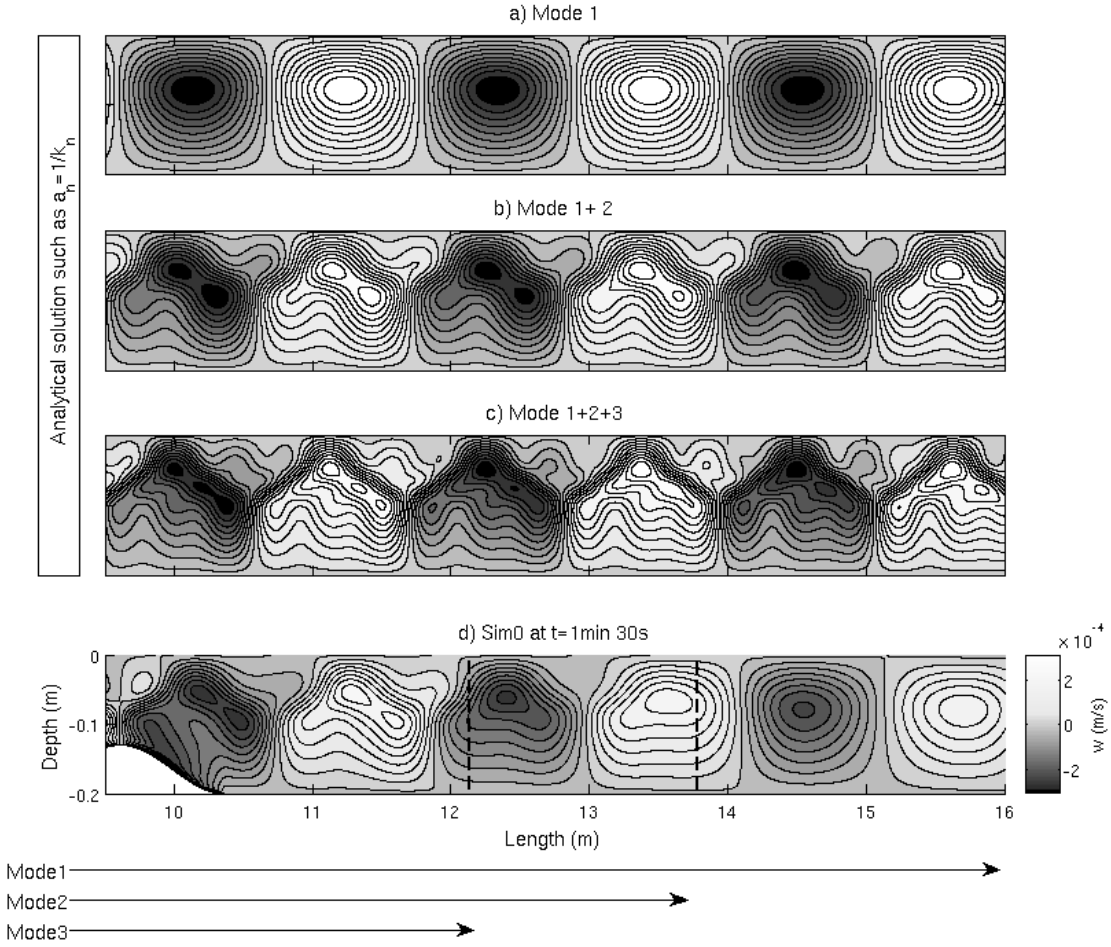

FIGURE 2 - Spatial structure of the first three modes calculated with the modal decomposition method for the vertical velocity component w and $a_n=1/k_n$. Parameters of the stratification profile are indicated in table 3 . White denotes positive values; black, negative ones.
a-spatial structure of the first mode only
b-spatial structure of the superposition of the first two modes
c-spatial structure of the superposition of the first three modes
*d-vertical velocity field in **Sim0** at t=5.6T: 20 streamlines, the velocity difference between two lines is $dw=4.10^{-5}$ m/s. Vertical dashed lines and arrows represent vertical modes travelled distance at t time, $x_n = c_n t$*

In figure 2-d, we can point out the contribution of the first and the second vertical mode: the first mode propagates faster than the second one (as shown by the arrows). However, the finner structure of the third vertical mode (additional lobe and thinner ray on figure 2-c) are not visible in **Sim0**. Near the strait (between 10 and 12 m), where the steady state is established, the vertical velocity field of **Sim0** fits extremely well with the superposition of the theoritical first and second mode structure (2-b). So there is a good agreement between the first and second theoretical vertical mode structure (a,b) and **Sim0** (d) vertical velocity field. After 12m, the structure associated to mode 2 is less visible, maybe because mode 2 dissipates relatively quickly with distance. Indeed, the dispersion parameter : $\mu_n = (\frac{H}{\lambda_n})^2$ with λ_n the wavelength of the vertical mode *n*, indicates a faster dissipation for mode 2 than for mode 1. To conclude, internal wave ray (IWR) angle, first and second vertical mode wavelength and celerity in **Sim0** correspond to theoretical values (table 3- Validation). So, in **Sim0**, it seems that only mode 1 and mode 2 escape from the strait.

To identify more precisely vertical modes generated and propagating in **Sim0**, we used two different statistical analyses. The goal is also to compare the amplitudes of each vertical mode in our simulations to expected solutions ($a_n \propto \frac{1}{k_n}$ & $a_n \propto 1$ – see section 1.c.i)

A singular value decomposition (SVD) analysis on the vertical velocity field is used to identify the dominant vertical modes (Appendix 3). Figure 3 represents time series (b) and vertical spatial patterns (a) associated to the first three empirical orthogonal functions (EOF). Two SVD analysis at different locations in space are presented: the first location is far from the strait (x_1=13.2m-plain lines) to have a long transitive time series, providing a better decorrelation of the first and second vertical mode, the other one is close to the strait (x_2=11.2m) to obtain a maximum amount of information with a longer time series (dotted lines). The first two EOF modes, in both locations, have the same periodicity as the tides (b-EOF1-EOF2). The third EOF mode, EOF3, has a pseudo-periodicity of 13.5-14.5 seconds, in both locations, fitting neither tidal or harmonic periodicity (*T*/2,*T*/3…). The percentage of variance explained associated to it is very small (3% at x_1, 2% at x_2). The signal is quite chaotic and the vertical spatial patterns associated (a-EOF3-dashed and dotted lines) do not match to any theoretical vertical mode profile (bold lines). Vertical spatial patterns associated to EOF1 (a-EOF1- dashed-dotted line) match approximately theoretical mode 1 vertical profile (bold line). Moreover, the initial time of the perturbation (b-EOF1- dashed-dotted line) fit vertical mode 1 arrival time (vertical line), $t_1 = \frac{x_1 - x_0}{c_1}$, at x_1 and x_2. It becomes less clear for EOF2 at x_2 point (b-EOF2-dotted line), where mode 1 and mode 2 are temporally close and more difficult to decorrelate. Indeed, vertical modes are not strictly independent from each other. There can be different kinds of interactions between them: advection of a higher mode by a lower one resulting in non-linear effects and property changes due to varying topography or varying stratification. That's why, there are some discrepancies between analytical vertical mode profiles (bold line-a) and EOF1 and 2 profiles (dashed and plain line-a). To conclude, SVD analysis succeeds to analyze the structure of the first two vertical modes. The percentage of variance explained associated to EOF1 (85% at x_1, 84% at x_2) is much higher than that of EOF2 (11% at x_1, 12% at x_2) indicating a domination of the first mode.

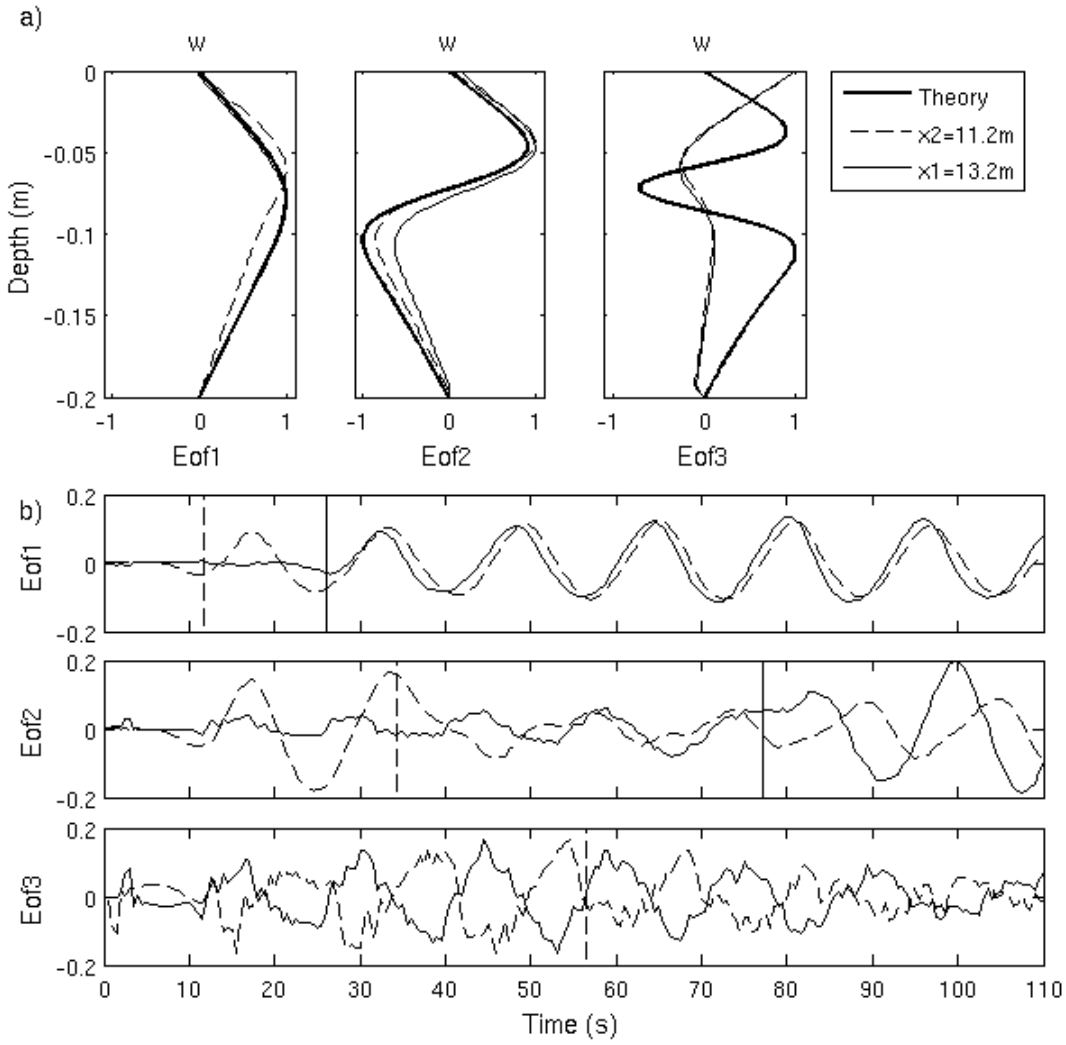

FIGURE 3 - ***Sim0*** *vertical velocity SVD analysis for 0-110 second period on two locations: (a) x_1=13.2m (b) x_2=11.2m;*

(a) plain and dashed lines: spatial pattern of the first three EOFs calculated respectively at x_1 and x_2 locations, Bold lines: First three vertical velocity modes profiles calculated with modal decomposition method,

(b) Plain and dashed lines: temporal variation associated to the first three EOFs respectively at x_1 and x_2 locations. Vertical lines: theoretical vertical modes arrival time, $t_n = \frac{x_1 - x_0}{c_n}$, at x_1 (dashed) and x_2 (plain).

The second statistical analysis is an orthogonal projection of the first four analytical vertical modes profiles calculated with the modal decomposition method, on vertical velocity field in **Sim0** in each spatial point and at each time step (Appendix 3). A time-space windows near the strait, but above flat bottom, have been selected where the first four vertical mode are theoretically propagating ($t \in [80s\ 110s]$, $x \in [10.4m\ 11.52m]$). A Fourier transform is performed along the time dimension. The resulting amplitude at the tidal frequency (f=1/T= 0.0625 s^{-1}) gives the associated amplitude of each vertical mode ($a_{n,w}$) in each spatial point (figure 4 – a)). Figure 4-b represent the spatial mean of vertical mode amplitude in the "near field" (solid line) and the vertical mode amplitude at its spatial boundaries positions (dotted line: x=10.4 m, dashed-dotted: x=11.52 m). The first and the second modes have significant amplitudes and the first mode is clearly dominant as

expected. The second mode amplitude decreases more rapidly than the first one, indicating a faster dissipation of the second mode. Mode 1 amplitude varies slightly with space (Fig. 4–a), possibly due to interaction with mode 2 (destructive or constructive) and reflection on the top and on the bottom of the pycnocline. A comparison is made between amplitudes deduced from the projection, $a_{n,w}$, and the normalized theoretical estimates ($a_n \propto 1/k_n$ & $a_n \propto 1$-bold lines). This suggested, as expected, that the most appropriate theoretical law is a decrease of the amplitude of the mode with the wavenumber. However, mode 3 and mode 4 theoretical amplitudes ($a_n \propto 1/k_n$) are overestimated because for large *n*, $a_n \propto {k_n}^{-3}$ (see 1.c.i).

To conclude, our numerical configuration succeeds to represent the modal decomposition of Gerkema and Zimmerman[34]. In subcritical topographic slope cases ($\gamma<\vartheta_\rho$), energy spreads not homogeneously between internal vertical modes, as expected, higher modes have smaller amplitudes. Most of the energy, generated by internal waves, is concentrated in the first mode.

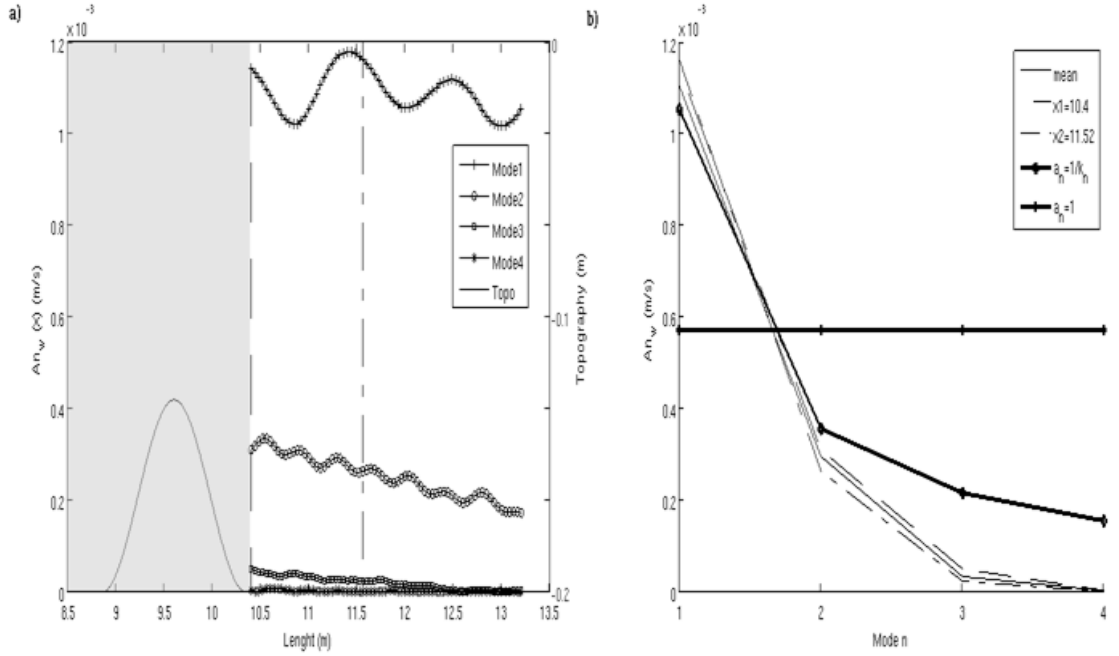

*FIGURE 4 - Orthogonal projection of the first four vertical velocity modes profiles calculated with modal decomposition method on **Sim0** vertical velocity field for 80-110 second period (without the transitive period inside the near field : 0-80s)*

(a) Spatial variation of the first four vertical modes amplitude (lines with markers); dashed and dashed-dotted vertical lines define the near strait field, shaded area: area of variable topography;

(b) First four vertical modes amplitude in the near field, dashed line: vertical modes amplitude at the position closest to the strait, dashed-dotted line: vertical modes amplitude at the position farthest to the strait inside the near field, plain line: average amplitude in the near field.Solid bold line with marker: rough theoretical estimate of vertical modes amplitude for subcritical topography ($a_{n,th}=1/k_n$ -circle marker-) and for supercritical topography ($a_{n,th}=1$ -cross marker-). These values are normalized such as: $\frac{a_{n,th}}{\|a_{n,th}\|}\left\|An_{w,mean}\right\|$.

4.2. Supercritical topography

A simulation, **Sim1**, with a supercritical topography (abrupt slope) is shown in Figure 5 (e) after 5.6 forcing period. This simulation differs from **Sim0** only by the strait width ($\lambda_r = 0.5m$) hence the topographic slope angle, γ.

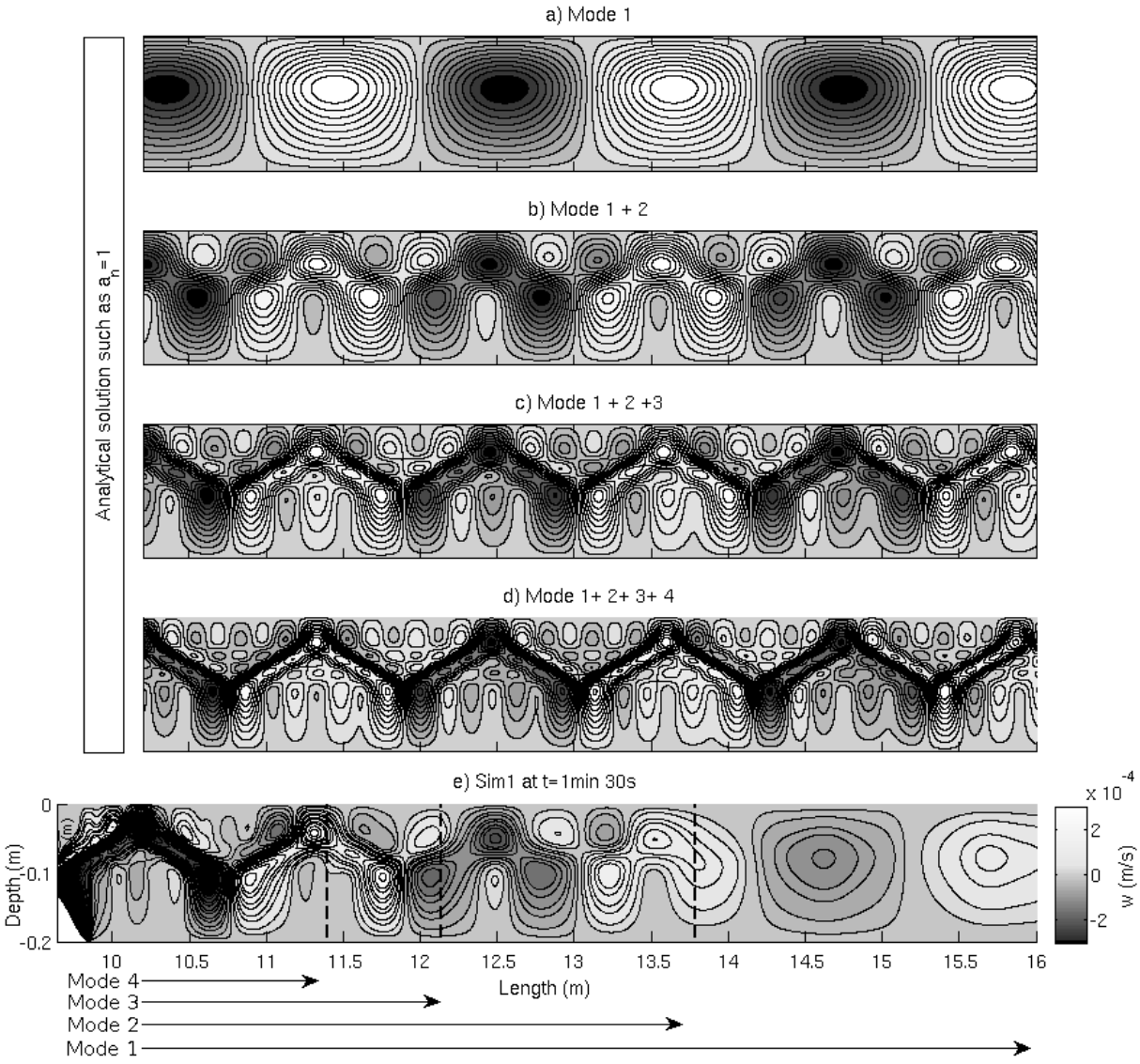

FIGURE 5 - Spatial structure of the first four modes calculated with modal decomposition method for the vertical velocity component, w, and a_n=1. Parameters of the stratification profile are indicated in table 3 . White denotes positive values; black, negative ones.

(a) spatial structure of the first mode only
(b) spatial structure of the superposition of the first two modes
(c) spatial structure of the superposition of the first three modes
(d) spatial structure of the superposition of the first four modes
*(e) vertical velocity field in **Sim1** at t=5.6T: 20 streamlines, the velocity difference between two lines is dw=4.10^{-5} m/s. Vertical dashed lines and arrows: vertical modes travelled distance at t time, $x_n = c_n t$*

The first four plots (a,b,c,d) of figure 5 are vertical velocity analytical fields calculated according to our stratification profile ($\Delta\rho$, $\delta\rho$,h_ρ,H) and the forcing periodicity (T) with vertical mode decomposition method. This time, as the topography is supercritical, we assume comparable amplitudes for all vertical modes ($a_n \propto 1$).

The first plot (a) shows only the first vertical mode and in each following plot we superimposed one additional vertical mode so the fourth plot (d) finally shows the first four vertical modes. The bottom plot (e) represents the vertical velocity output from **Sim1** at t=5.6T.

On figure 5-a-b-c-d, we can see the constructive superposition of vertical modes in the pycnocline and the apparition of the structured ray. The greater the number of modes involved, the finer the structure of the ray becomes. In figure 5-e, we can point out the contribution of each vertical mode during the transition period: the higher modes do not propagate as fast as the lower modes (as shown by the arrows). In this transition area, the first three modes are cleary distinguishable. There is a good agreement between the theoretical vertical mode structures (a,b,c,d) and the vertical velocity field in **Sim1** (f). However, near the strait, where the steady state is already established, the superposition of the vertical mode and the apparition of the ray structure render more difficult the identification of each vertical mode involved. The associated density field and isopycnal vertical displacements show that the first three modes have significative amplitude, hence energy seems concentrated in these three modes. So it is difficult to determine which of these vertical modes are the most energetic but we can clearly identify the structure of the first three vertical modes on density and velocity field. Moreover, internal wave ray (IWR) angle, vertical mode wavelength and celerity in **Sim1** for the first three modes correspond to theoretical values (table 3 – validation-).

The modal selectivity appears to be more complex than the criterion: $a_n \propto 1$. However, the vertical velocity field in **Sim1** (Fig. 5-e) corresponds more closely to an energetic equidistribution between vertical mode ($a_n \propto 1$- Fig. 5-c-d) than to a decrease of the amplitude of the mode with the wavenumber ($a_n \propto \frac{1}{k_n} - \mathrm{Fig.\ 2-c}$). In other words, in this supercritical topographic case, theoretical correlation with experiment **Sim1** is better for $a_n \propto 1$, than for $a_n \propto \frac{1}{k_n}$ as expected.

A singular value decomposition (SVD) analysis on the vertical velocity field is used to identify the dominant vertical modes. Figure 6 shows time series (b) and vertical spatial patterns (a) associated to four EOF modes. Two SVD analysis at different locations in space are presented: the first location is far from the strait (x_1=13.2m, plain lines) to have a long transition time series, providing a better decorrelation of the first and the second vertical mode, the other one is close to the strait (x_2=11.2m, dashed lines) to obtain a maximum amount of information with a long time series. At x_2=11.2m (dashed lines), all EOF modes (b), have the same periodicity as the tides. Spatial patterns of EOF 3 and 4 (a-EOF 3-4- dashed lines) correspond respectively to theoretical vertical modes 3 and 4 (bold lines). There are some discrepancies between mode 1 and mode 2 analytical vertical mode profiles (bold line) and EOF 1 and 2 profiles (dashed line). A signal leakage is observed between these

different EOF modes, i.e. an unwanted signal before mode arrival time, phased with the previous EOF mode (b-EOF 2-3-4). Nevertheless, the phase of the signal change after the mode arrival time, so each of these EOF modes seems to be related to a different vertical mode. At x_1=13.2m, there is a better correlation between EOF1,2 (a-EOF1-2-plain line) and analytical first and second vertical modes. To conclude, SVD analysis succeeds in analyzing the structure of the first four vertical modes. However, no dominant vertical mode can be extracted: the values of the percentage of variance explained associated to EOF modes are less reliable due to this mixing of signal.

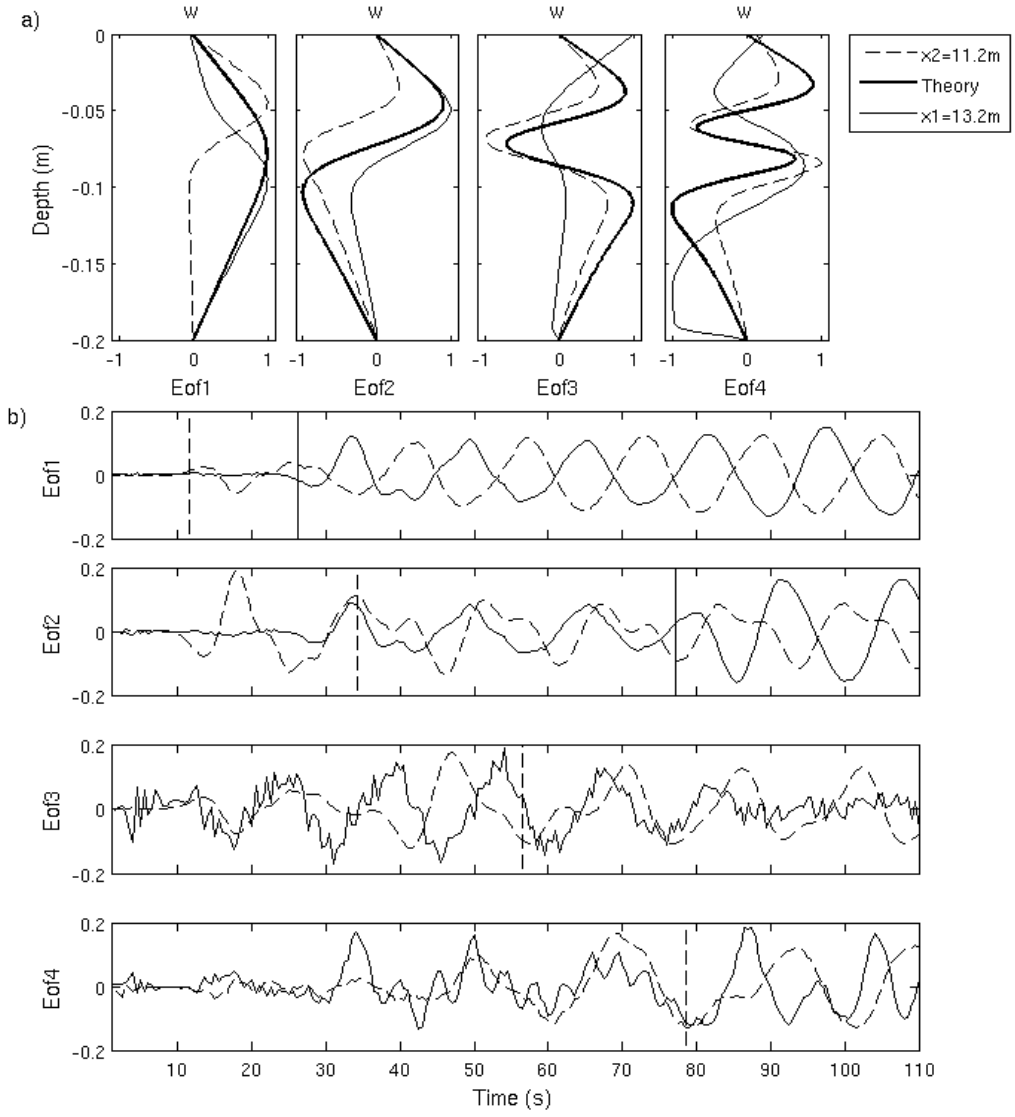

*FIGURE 6 - **Sim1** vertical velocity SVD analysis for 0-110 second period on two locations: (a) x_1=13.2m (b) x_2=11.2m;*

(a) plain and dashed lines: spatial pattern of the first four EOFs calculated respectively at x_1 and x_2 locations, Bold lines: First four vertical velocity modes profiles calculated with modal decomposition method

(b) Plain and dashed lines: temporal variation associated to the first four EOFs respectively at x_1 and x_2 locations. Vertical lines: vertical modes arrival time, $t_n = \frac{x_1 - x_0}{c_n}$, at x_1 (dashed) and x_2 (plain).

Figure 7–a represents the evolution of the first four vertical mode amplitude ($a_{n,w}$) of **Sim1** as a function of space calculated with the method of orthogonal projection. Figure 7-b represents the spatial mean of vertical mode amplitude in the near field (solid line) and the vertical mode amplitude at its spatial boundaries positions (dashed line: *x=10 m*, dashed-dotted: *x=11.16 m*). The main difference with **Sim0** is that the second mode has the largest amplitude near the generation area. Moreover, mode 3 and mode 4 have also significant amplitudes in this case. So, in this supercritical case, even if the first four modes have significant amplitudes, the assumption of identical amplitude for all vertical modes ($a_n \propto 1$) seems to be rather crude. In particular, this law does not predict the largest magnitude of the second mode near the generation zone. This could be the effect of a particular selectivity mechanism or a resonating character of the generating mechanism in **Sim1**. In addition, high modes dissipate more rapidly than the first mode.

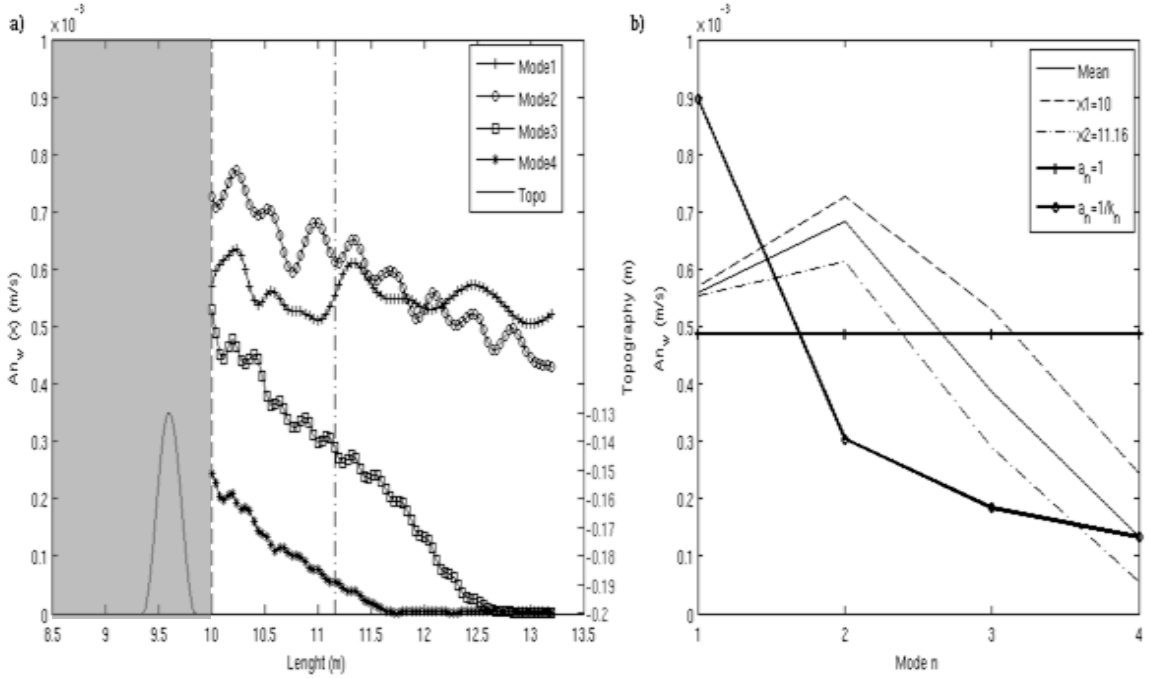

*FIGURE 7 - Orthogonal projection of the first four vertical velocity modes profiles calculated with modal decomposition method on **Sim1** vertical velocity field for 80-110 second period*

(a) Spatial variation of the first four vertical modes amplitude (lines with markers) : dashed line and dashed-dotted line define the near strait field, shaded area: area of variable topography.

(b) First four vertical modes amplitude in the near field, dashed line: vertical modes amplitude at the position closest to the strait, dashed-dotted line: vertical modes amplitude at the position farthest to the strait inside the near field, plain line: average amplitude in the near field.Solid bold line with marker: rough theoretical estimate of vertical modes amplitude for subcritical topography (a_n=1/k_n -circle marker-) and for supercritical topography (a_n=1 -cross marker-). These values are normalized such as: $\frac{a_{n,th}}{\|a_{n,th}\|}\|An_{w,mean}\|$.

To conclude, in this supercritical topography case, the numerical configuration succeeds also in representing the modal decomposition of Gerkema and Zimmerman[34]. In this case, energy spread more homogeneously between internal vertical modes: higher modes have also an influence on the vertical velocity field structure and significant amplitudes ($a_n \neq 1/k_n$). Moreover, the orthogonal

projection seems to indicate a mode 2 selectivity mechanism. So, the question of the partitioning of the energy between vertical modes with possible selectivity mechanism or resonating character is raised. This is in line with the resonating character highlighted by Gerkema and Zimmerman[38] and Vlasenko *et al.* [17] for small and large subcritical topography. Vertical modes do not dissipate at the same rate as observed in **Sim1** (figure 7-a) and indicated by the dispersion parameter ($\mu_n = (\frac{H}{\lambda_n})^2$). So energy radiated by each mode will drive turbulence dissipation at different locations. In particular, the first three modes propagate away from the generation zone and therefore induce remote mixing contrary to higher modes causing, in turn, local mixing. It is thus crucial to understand and quantify the partitioning of the energy between vertical modes.

4.3. Topographic control on vertical mode generation

Several numerical tests are performed to understand what can influence the energy partition between internal vertical modes in supercritical topography cases. Four potential parameters play a role on the vertical mode generation: the density jump, $\Delta\rho$, the pycnocline thickness, $\delta\rho$, tidal periodicity, T and strait width, λ_r. In the present work, the topographic selection criterion of Dossmann *et al.*[9] is tested. The authors demonstrate a topographic control mechanism for primary internal solitary wave generation. To generate a topographically induced internal solitary wave in a pycnocline, its wavelength λ and the ridge bottom width, λ_r, must have the same order of magnitude: $\frac{\lambda}{\lambda_r} \approx 1$. If we use a similar topographic selection criterion applied for vertical mode in a pycnocline: $\frac{\lambda_n}{\lambda_r} \approx 1$, the most energetic mode (n) would be selected by the strait width. Moreover, this criterion corresponds to Vlasenko's[17] condition of maximal modal amplitude in subcritical topography cases (section 1.c.i).

In **Sim1**, $\frac{\lambda_1}{\lambda_r} \approx 4.4$, $\frac{\lambda_2}{\lambda_r} \approx 1.5$, $\frac{\lambda_3}{\lambda_r} \approx 0.9$ and $\frac{\lambda_4}{\lambda_r} \approx 0.6$, indicating a possible selectivity of the second and the third mode. Yet, as we show in section 2.b, the first three vertical modes have significant amplitude and the mode 2 amplitude is the largest. So a topographic selection criterion close to or superior to one seems to indicate significant amplitude.

To test our criterion, we perform a second simulation, **Sim2**, such as $\frac{\lambda_4}{\lambda_r} \approx 1$ and $\frac{\lambda_1}{\lambda_r}$, $\frac{\lambda_2}{\lambda_r}$, $\frac{\lambda_3}{\lambda_r}$ are superior to 1 (table 3). For that, we changed only one initial condition parameter: the strait width ($\lambda_r = 0.3m$) so the tidal forcing and the stratification are the same in the three simulations (**Sim0**, **Sim1** and **Sim2**). Consequently, tidal velocity, modal wavelength and celerity are also the same.

We performed an orthogonal projection of the first four analytical vertical modes on the vertical velocity field in **Sim2** in the same time-space windows: ($t \in [80s\ 110s], x \in [10m\ 11.16m]$). Figure 8–a represents the resulting vertical mode amplitudes ($a_{n,w}$) in each spatial point. Figure 8-b represent the spatial mean of vertical mode amplitude in the "near field" (solid line) and the vertical mode amplitude at its spatial boundaries positions (dashed line: x=10 m, dashed-dotted: x=11.16 m). In **Sim2**, it is still the second mode which has the largest amplitude near the generation area.

However, in this case, modes 3 have larger amplitude than mode 1 close to the strait. Moreover, just next to the strait, modes 2 and 3 have slightly the same amplitude. Looking more closely, at *x*=10m, the amplitude of mode 3 in **Sim2** ($A_{M3,Sim2}$=5.4.10^{-4} m/s, Figure 8-b) is almost the same than in **Sim1** ($A_{M3,Sim1}$=5.3.10^{-4} m/s, Figure 7-b) but the amplitude of mode 1 in **Sim2** is smaller. Nevertheless, mode 4 amplitude in **Sim2** is larger than in **Sim1** ($A_{M4,Sim2}$=3.3.10^{-4} m/s > $A_{M4,Sim1}$=2.4.10^{-4} m/s). This result confirms our assumption: to reach the maximum amplitude of a mode *n*, its wavelength, λ_n, must be of the same order than the ridge width, λ_r: $\frac{\lambda_4}{\lambda_r}, Sim1 \approx 0.6$; $\frac{\lambda_4}{\lambda_r}, Sim2 \approx 1.05$. The dissipation rates of high modes are still much higher than mode 1 dissipation rate especially for modes 3 and 4. This strong dissipation rate may be also related to the reflection on the top and on the bottom of the pycnocline or to interaction between other vertical modes which could result in energy exchange or loss.

In **Sim2**, which is more supercritical than **Sim1** ($(\theta_{th}/\gamma)_{Sim2} < (\theta_{th}/\gamma)_{Sim1}$, table3), energy spread even more homogeneously between the first four vertical modes which have all significant amplitudes. The most energetic vertical modes are the second and third ones. The amplitude of mode 4 is maximal. A topographic selection criterion for a mode *n*, near 1 or superior to 1, seems to indicate that this mode *n* has significant amplitude, at least, next to the generation area.

The vertical and horizontal resolutions are also questionable. Vertical modes cannot be represented numerically if the horizontal resolution is larger than half its wavelength. The vertical resolution of the pycnocline must be also high enough to represent the vertical structure of higher modes. This is a reason why the study is focused particularly on the first four modes.

Other tests with different pycnocline thickness, δρ, and different topographic blocking degree, B have been done (not shown here). The topographic control on vertical mode generation has also been observe in thinner pycnocline cases ($\delta\rho \in [0.02\ 0.06\ m]$) and located further from the strait (B $\in [0.58\ 0.94]$). In these tests, mode 2 amplitude can also be larger than mode 1 amplitude under the proper conditions ($\frac{\lambda_2}{\lambda_r} \approx 1, \frac{\lambda_1}{\lambda_r} \gg 1$) .

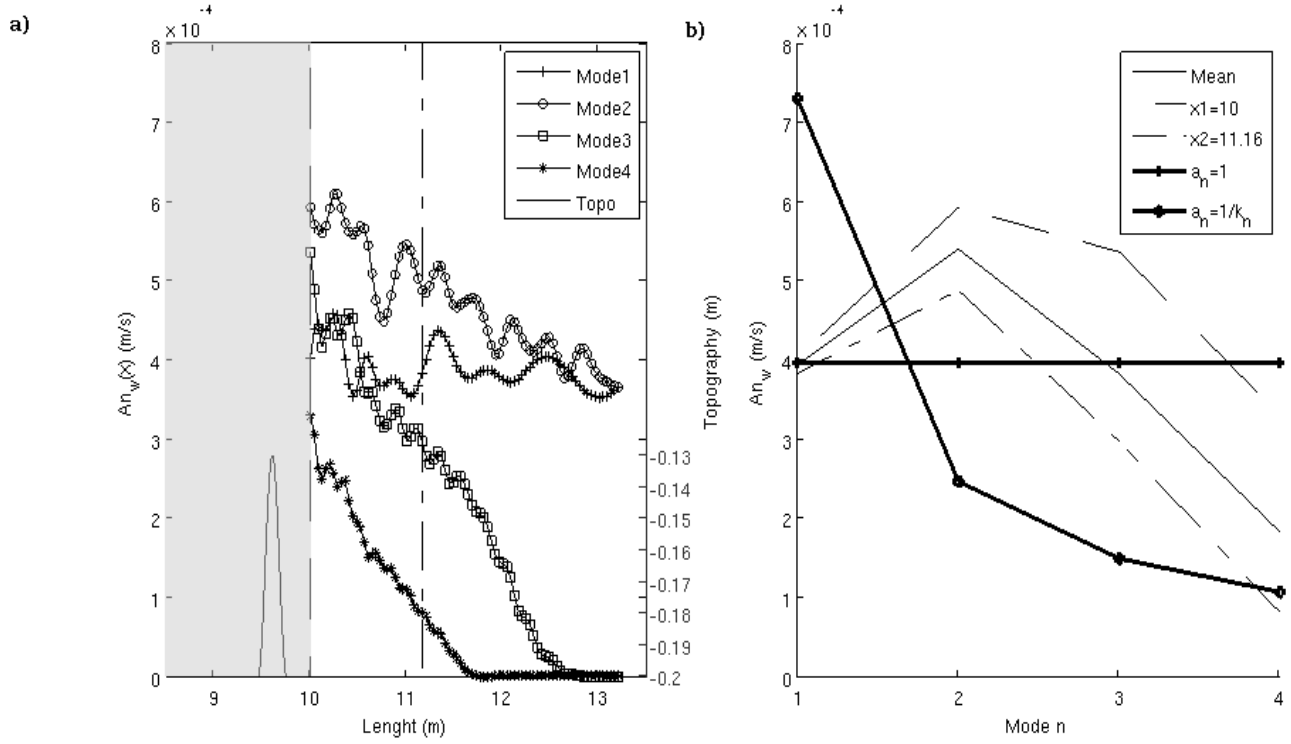

*FIGURE 8 - Orthogonal projection of the first four vertical velocity modes profiles calculated with modal decomposition method on **Sim2** vertical velocity field for 80-110 second period*

(a) Spatial variation of the first four vertical modes amplitude ((lines with markers): dashed line and dashed-dotted line define the near strait field, shaded area: area of variable topography.

(b) First four vertical modes amplitude in the near field, dashed line: vertical modes amplitude at the position closest to the strait, dashed-dotted line: vertical modes amplitude at the position farthest to the strait inside the near field, plain line: average amplitude in the near field.Solid bold line with marker: rough theoretical estimate of vertical modes amplitude for subcritical topography ($a_n=1/k_n$ -circle marker-) and for supercritical topography ($a_n=1$ -cross marker-). These values are normalized such as: $\frac{a_{n,th}}{\|a_{n,th}\|}\left\|An_{w,mean}\right\|$.

To conclude, in supercritical slope cases, a topographic control or resonance character similar to the one of the generating mechanism above small bottom (subcritical topography) is recovered. It is characterized by the ratio of the *n* mode wavelength λ_n to the ridge bottom width λ_r. Indeed, the condition of maximal modal amplitude of Vlasenko *et al.*[39], for subcritical topography, applies also in our supercritical topography cases. By contrast, for fixed values of *l*, the amplitudes a_n , are no more proportional to k_n^{-1} (or k_n^{-3} for large *n*). Indeed, in supercritical cases, the amplitudes of higher modes are significant and can even exceed the amplitudes of the lowest modes (as in **Sim1** and **Sim2**). Nevertheless, the assumption of a similar amplitude for all vertical modes (a_n =1) in supercritical cases, is too crude as it does not take into account this topography control on vertical mode generation.

5. Supercritical and nonlinear flow

The objective of this section is to understand better the relationship between hydraulic control and ISWs formation. We select four typical internal wave behaviors among all the regimes and simulations performed to illustrate this relationship. In order to create conditions for hydraulic control, we perform, in a shallow supercritical strait($B = 0.94$, $\frac{\theta_p}{\gamma} < 1$), simulations with strong tidal forcing ($\frac{U_{max}}{c_2} \geq 1$) and a thin pycnocline ($\delta\rho^* = 0.1$) except for the last configuration (table 4).

		Non-linear Regime $\varepsilon \geq 0.018$			
		Mode 2 Hydraulic Control $F_2 \geq 1$ & $\lambda_2/\lambda_r \approx 1$	Mode 1 Hydraulic control $F_1 \geq 1$		
		Sim3 *M2 & M1 ISWs*	**Sim4** *M1 ISWs & breaking*	**Sim5** *Linear M1*	**Sim6** *Quasi-steady lee wave*
initial conditions (I.C.)	h_ρ, h_0	0.03, 0.15			**Sim1**'s I.C.
	Δρ, δρ	8, 0.02			
	λ_r	0.5			
	T	40	24	10	
	A	0.012	0.033	0.02	0.3
Regime parameters	B	0.94			0.7
	A/ λ_r	0.024	0.066	0.04	0.6
	θ_{th}/γ	0.15	0.25	0.60	0.47
	ε	0.018	0.05	0.03	0.21
	λ_1/λ_r	3.2	1.9	0.7	4.4
	λ_2/λ_r	0.9	0.5	0.2	-
	λ_3/λ_r	0.5	0.3	0.1	-
	$\frac{u_{max}}{c_{n_{th,H}}}$	0.2	0.9	1.5	1.3
		0.9	3.3	5.7	-
	$\frac{u_{max}}{c_{n_{th,D}}}$	0.4	1.4	2.2	1.8
		1	3.8	6	-
Post-analysis	$\max(F_{n,D_{x0}})$	0.5	1.5	1.8	1.9
		1.3	4.1	4.9	-
	$\max(F_{n,H_{x0}})$	0.3	0.97	1.3	1.4
		1.1	3.6	4.7	-

TABLE 4–Numerical and physical parameters for supercritical an non-linear flow

The four following regimes are non-linear (ε≥0.018). The topographic selection criterion varies in the different simulations; consequently, the energy is injected preferentially in different internal vertical modes. The influence of this parameter is discussed in detail as well as the possible nonlinear interactions between these vertical modes. These three non-dimensional parameters: ε, $\frac{\lambda_2}{\lambda_r}$, F_n are adopted to describe the nonlinear regimes. Special attention will also be given to local wave breaking processes. Indeed, in supercritical cases, hydraulic jump is believed to break directly near the topography due to nonlinearities in the generation process itself. However as the processes are very non-linear and sensitive to small changes in local forcing, a large number of caveats comes into play before we fully understand dissipation at supercritical sites (Klymak et al.[18]).

5.1. A mode 2 hydraulic control

First, simulation (**Sim3**), with hydraulic control on the second vertical mode is shown in figure 9. In this mode 2 hydraulic control regime, modes 2 are generated only on one side of the strait at each half-tidal period due to hydraulic control and disintegrate in periodic trains of two ISWs. But modes 1 are not subject to hydraulic control.

In this configuration, energy is injected preferentially in mode 2 ($\frac{\lambda_1}{\lambda_r} \approx 3.2$, $\frac{\lambda_2}{\lambda_r} \approx 0.9$ - table 4). The tidal period is 40 s. Figure 9-a represents the evolution of vertical displacements, in space and time, of the isopycnal line ρ=1041 Kg.m^{-3} located at the top of the pycnocline: light colors correspond to a positive isopycnal elevation and dark colors to an isopycnal depression. To represent the vertical evolution of an isopycnal line, a variable change is performed offline by a tracking method (ρ(z)→z(ρ)). This diagnostic have been performed for several isopycnal lines, the most informative have been selected. Arrows represent theoretical celerity of the first and second vertical modes, propagating along this isopycnal surface. White and black bold contour lines correspond to $F_2 = -1$ and $F_2 = 1$, respectively, in other words, mode-2 hydraulic control area. The mode 1 Froude number is not represented because there is no mode 1 hydraulic control: $F_1 < 1$. Figure 9-b indicates time evolution of the maximal vertical value of the fluid velocity at the shallowest strait depth, x_0: $max_z\, U(x_0, t)$ so this plot indicates time evolution of tidal intensity and orientation at the shallowest strait depth. Finally, figure 9-c shows a pycnocline's vertical section at t=1.25T, corresponding to the dashed line on Figure 9a-b. This gives us information about internal wave's vertical density structure.

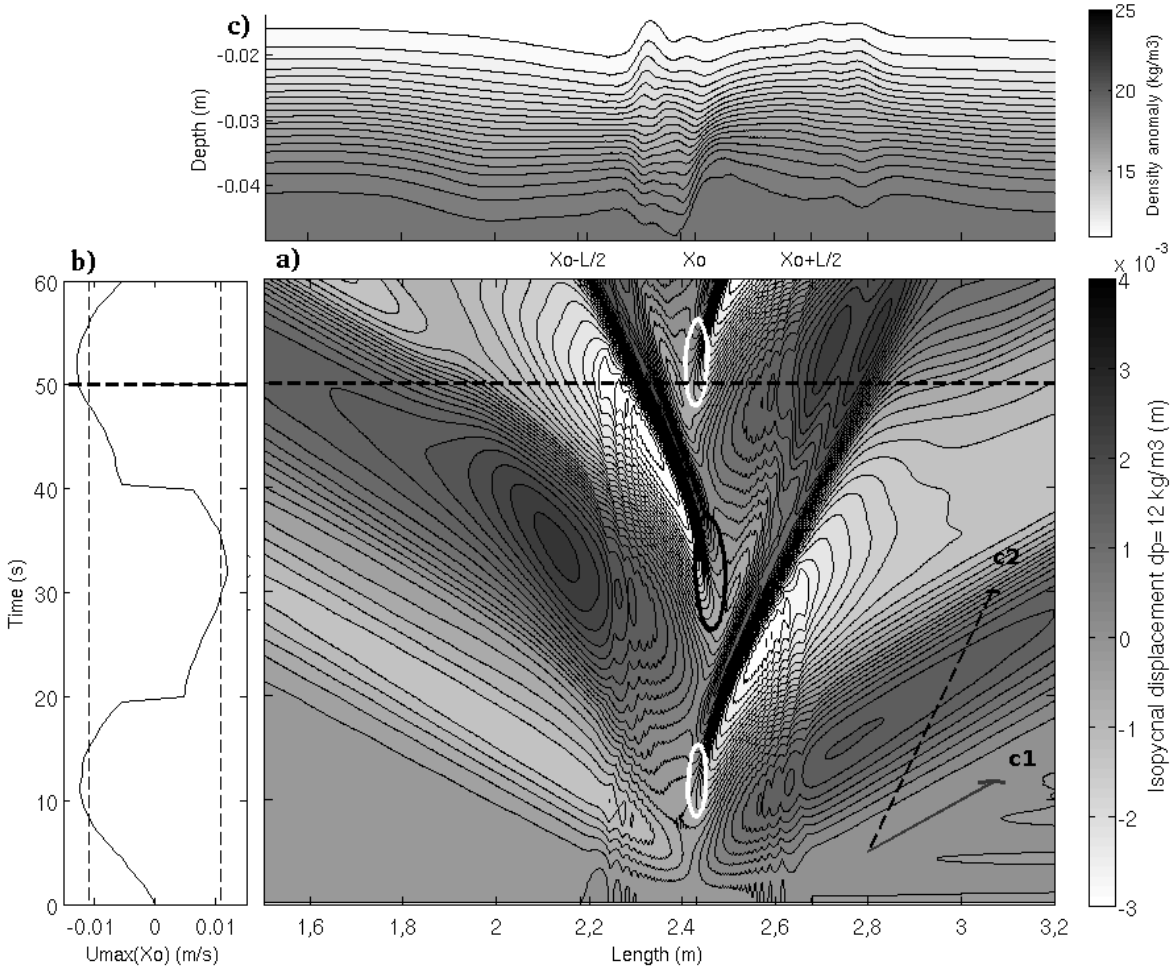

FIGURE 9 – a) Space-time diagram of the vertical isopycnal displacement for δ ρ=12 kg/m^3(located at the top of the pycnocline) in ***Sim3****. Arrows indicate the speed of the first two normal modes calculated with modal decomposition method (c_1= 0.04 m/s, c_2= 0.011 m/s). White and black contour lines locate mode 2 Froude number of minus one and one. Horizontal bold dashed line locates temporally the vertical section of the pycnocline.*
b) Temporal evolution of the fluid maximum velocity located just above the ridge (at x_0); vertical dashed lines: mode 2 celerity; horizontal bold dashed line locates temporally the vertical section of the pycnocline.
c) Vertical section of the pycnocline at t=1.25T=50s

Two different waves propagate along this Isopycnal lines: faster waves emitted at each half tidal period, on each side of the strait and slower waves emitted during slack tide periods, only on one side of the strait. On the pycnocline vertical section, the slower waves are associated to an opposition of phase between the top and the bottom of the pycnocline whereas for the faster waves, all isopycnes are in-phase. Hence the slower waves have the structure and the celerity of mode 2 and the faster waves correspond to mode 1. Mode 2 Froude number become superior to one above the strait, at each half tidal period, so modes 2 are subject to hydraulic control. Moreover, mode 2-waves disintegrate into two trains of ISWs. In addition, it was shown that the condition of Mode 2 amplitude is close to maximal ($\frac{\lambda_2}{\lambda_r} \approx 0.9$). To characterize nonlinear behavior of first and second vertical modes, a SVD analysis is realized near the strait (at x_1=2.9 m). Figure 10 shows spatial

patterns and associated time series of the first and the second EOF modes. Spatial patterns indicate that first and second EOF (plain lines) correspond to mode-1 and mode-2 theoretical vertical structure (bold lines) respectively. In this way, time series provide information about nonlinearity of mode-1 and mode-2. Both time signals have a 40s-periodicity. Modes 1 show nonlinearity leading to a steepening of the rear wave face: sharper troughs and flatter crests. Although mode 2 is disintegrated into two trains of ISWs: mode 2 time series present two depressions.

Near the strait, SVD analysis indicates that the first and second vertical modes signals have a similar intensity. The intensity of the second mode decreases when a SVD analysis is performed farther from the strait. This indicates a decrease of the mode-2 amplitude during the propagation, so a possible mode-2 ISW energy loss. In linear cases (as in section 2) mode 2 amplitude decreases and depends on the parameter of dispersion: $\mu_n = (\frac{H}{\lambda_n})^2$, so mode 1 will propagate farther than mode 2. Nevertheless, ISWs are supposed to conserve their energy. Many reasons can explain this signal amplitude decrease:

- Formation of many small amplitude troughs due to dispersion effects, leading to the signal loss: the mode-2 ISWs train is not observable any more but there is no energy loss. The energy is transferred to small scales or the energy is numerically dissipated.

-Non linear interactions with mode-1 ISW: when a mode-1 catch up a mode-2 ISW, it is possible that nonlinear energy interactions happen between them. This advection process has been observed in different area. In the northern South China Sea, short internal waves riding on second mode ISW have been observed, hypothetically generated by the overtaking of the second mode ISW by a first mode ISW (Guo et al[40]).

- Energy distribution change redirected to the mixing or the bottom layer: this mechanism occurs in the secondary generation case. Indeed IWR reflect on the top and on the bottom of the pycnocline, this can lead to non-linear interaction or energy exchange with the mixing or the bottom layer. This can lead, for example, to a change of mode 2 ISW vertical structure, hardly traceable with SVD analysis.

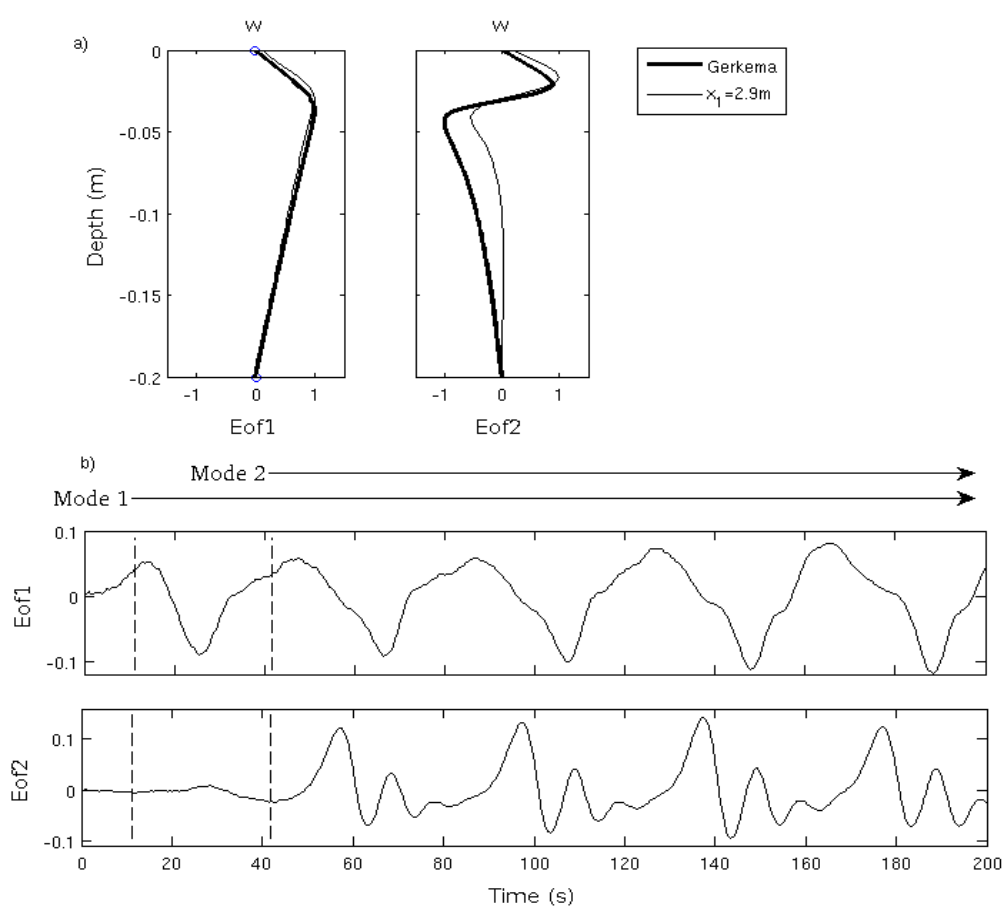

*FIGURE 10- **Sim3** vertical velocity SVD analysis for 0-200 second period on the location: x_1=2.9 m*

(a) plain lines: spatial pattern of the first and the second EOF analysis, Bold lines: First two vertical velocity modes profiles calculated with modal decomposition method,

(b) Vertical dashed line and arrows: vertical modes arrival time, $t_n = \frac{x_1 - x_0}{c_n}$, at x_1 point. Plain lines: temporal variation associated to the first and second EOF.

To conclude, in this mode 2 hydraulic control regime, mode 2 are generated only on one side of the strait at each half-tidal period due to hydraulic control and disintegrate in periodic trains of two ISWs. Modes 1 are generated each half tidal period, on each side of the strait and do not disintegrate into ISWs train. Mode-2 ISWs radiate a non-negligible amount of energy. The processes responsible for the "fast dispersion" of mode-2 ISWs are multiple and so difficult to dissociate.

To generate mode 2 ISWs in supercritical straits, many conditions must be fulfilled. The first condition is related to the topography selection criterion: an important part of the energy must be injected in mode 2, this is the case when $\frac{\lambda_2}{\lambda_r} \approx 1$. The second condition is related to the non linearity parameter ε, linked to the conversion efficiency from horizontal to vertical displacement by the ridge, non linear effects and ISWs appear for ε≥0.018. Moreover, Mode 2 ISW propagation distance depends on multiples processes of interaction with its environment, as advection by another ISW or ocean circulation. These effects are difficult to take into account in mixing parameterizations. At that point, the best to localize precisely the mixing induced by ISWs in numerical simulation is to resolve explicitly ISW dynamics and environmental factors.

5.2. A mode 1 hydraulic control with breaking and instabilities

A simulation (**Sim4**), with wave breaking above the strait is shown in figure 11. Modes 2 and modes 1 are subject to hydraulic control, when the hydraulic jump is released, it breaks above the strait and modes 1 disintegrate in periodic trains of two ISWs.

Only tidal forcing parameters vary from **Sim3** : T =24 s, A =3.3.10^{-2} m such as U_{max}/c_1=0.9 and U_{max}/c_2=3.3 (table 4). So this regime is highly nonlinear: ε=0.05 and we can additionally expect a hydraulic control of the first and second vertical mode. Moreover, energy is injected preferentially in the first mode ($\frac{\lambda_1}{\lambda_r} \approx 1.9$, $\frac{\lambda_2}{\lambda_r} \approx 0.5$). Figure 11-a represent the displacement, in space and time, of the isopycnal line ρ=1044 kg.m^{-3} located at the top of the pycnocline. The strait is located at $\boldsymbol{x_0}$ =1.54 m. Black and white bold contour lines still correspond to a mode 2 Froude number of 1 and -1. Figure 11-c depicts time evolution of fluid velocity at the shallowest strait depth (h=D) and dashed lines represent two values of mode 1 celerity: $c_{1,H}$ (calculated in deep water so for a depth of h=H=0,2m) and $c_{1,D}$ which is mode 1 celerity interpolated at the shallowest strait depth so for a total depth of D (h=D=0.05m) (section 1.c.ii).

Two different internal wave modes propagate along this isopycnal line, both generated during slack tidal periods and only on one side of the strait. The slower waves have mode 2 structure and celerity. The faster one, corresponding to mode 1-wave, disintegrates into two trains of ISWs, and propagates far from the strait. Mode 2 dissipates rapidly, more rapidly than in **Sim3**. Bold contour indicate a large spatial area of mode-2 hydraulic control leading to a fast dissipation of mode 2: when tides reverse, mode 2 has not propagated far enough from the strait and is still in the mode 2 hydraulic control spatial area so it is advected backward by tidal current and losses its energy . This energy loss can be related to an energy exchange with the tidal current. Indeed, Vlasenko and Stashchuk[41] highlight a mechanism of suppression or amplification of internal waves by a current over an inclined bottom in supercritical fluid condition. He showed, in particular, that the internal waves lose energy when they propagate downslope–upstream. Here, mode 2 is still above the strait (x<1.79) propagating downslope (away from the strait) and it is advected backward by tidal current (the tidal current is upstream and supercritical regarding to mode 2 celerity). So, the amplitude of the wave, which is decelerated by the presence of the strong barotropic flux, rapidly decreases. Moreover, in this configuration, mode 2 is not selected by the topography width so its initial amplitude is reduced. In contrast, when the mode 1 is propagating downslope, the tidal current is downstream so the amplitude of the first mode accelerated by the current is increased. Besides the topographic control on vertical mode generation, there is also a hydraulic selectivity on vertical mode propagation characterized, in particular, by the modal Froude number.

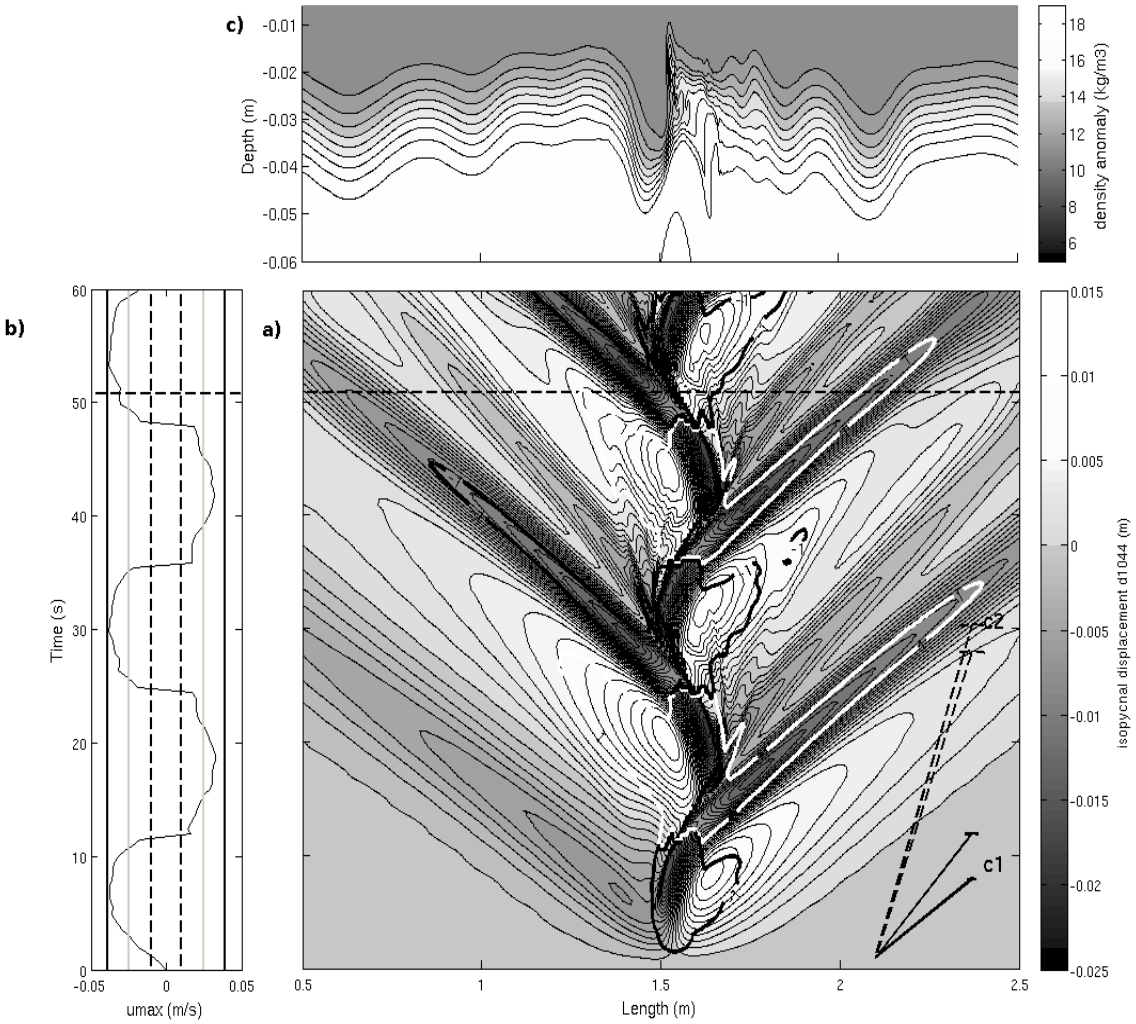

*FIGURE 11 –a) Space-time diagram of the isopycnal displacement d1044 for ρ=1044 kg/m^3 (located at the top of the pycnocline) in **Sim4**. Arrows indicate the speed of the two fastest normal modes calculated with modal decomposition method (c_1= 0.039 m/s, c_2= 0.01 m/s). Black and white contour lines locate hydraulic control of the second vertical mode.*
b) Temporal evolution of the fluid maximum velocity located just above the ridge; vertical lines: (dashed) mode 2 celerity,(plain bold) $c_{1,H}$, (plain gray) $c_{1,D}$, horizontal bold dashed line locates temporally the vertical section of the pycnocline.
c) Vertical section of the pycnocline at t=50,8 s

The mode 1 Froude number is inferior to one (table 4- $max\ (F_{n,H_{x0}}) < 1$) indicating no mode 1 hydraulic control. Nevertheless modes 1 are emitted only on one side of the strait at each half tidal period indicating possible mode 1 hydraulic control. The maximal values of the fluid velocity are located just above the strait, above varying topography. So, in this area the value of mode 1 celerity is questionable. The assumption of a flat bottom with a depth of *H*=0.2 m, made to calculate this celerity, is no longer valid. Moreover, when the hydraulic jump is released and propagates above the strait, the topography change, impacts its wavelength, celerity and amplitude. Thus, another assumption is made to characterize mode 1 celerity above the strait, considering a bottom with a depth of *h=D*=0.05m (so the shallowest depth of the strait). If we consider this new mode 1 celerity,

$c_{1,D}$=0.025 m/s (section 1.c.ii), the maximal Froude number value is superior to one ($max\ (F_{n,D}{}_{x0}) >$ 1-Table 4-), so there is a mode 1 hydraulic control.

A new phenomenon appears in this regime: at each tidal reversal, the hydraulic jump is released and breaks above the strait. Figure 11-c shows this breaking phenomenon: during the previous tidal period a hydraulic jump was formed on the lee side of the strait, it is released, propagates leftward (on figure 11-a) and then breaks above the strait. The nature of the instability leading to this breaking is questionable. At least, two kinds of instabilities can be responsible: Kelvin-Helmholtz instability due to shear current and characterized by a Richardson number inferior to 0.25 or a kinematic instability characterized by a fluid velocity superior to the hydraulic jump propagation velocity. If we consider that the hydraulic jump has a mode 1 celerity interpolated at *D*, the kinematic instability condition is reached during the overturning event t_B : $max_z\ U(x_0, t_B) > c_{1,D}$. The overturning event is defined by Vlasenko and Hutter[42] as the moment at which the top of the propagating baroclinic bore outstripped the wave trough. In this situation the heavier and denser water penetrates into the relatively light water layers and falls down to the wave trough. Nevertheless, before the overturning event, the buoyancy frequency turns negative with the steepening of the hydraulic jump, at the same time; the corresponding Richardson number is inferior to 0.25. So, the Richardson criterion is reached before the kinematic instability condition. For a mechanism of strong wave breaking up to overturning event, a kinematic instability seems to be responsible rather than a shearing instability, as was suggested by Kao et al.[43].

To conclude, in this breaking regime, mode 2 and mode 1 are generated only on one side of the strait at each half tidal period due to hydraulic control and mode 1 disintegrates in periodic trains of two ISWs. Moreover hydraulic jump breaks above the strait and leads to strong local mixing. This breaking event is due to mixed kinematic instability and Kelvin-Helmholtz instability.

5.3. A mode 1 hydraulic control without ISWs formation

A simulation (**Sim5**), with supercritical topography and supercritical flow but without ISWs trains formation is shown in figure 12. Only tidal forcing parameters vary from **Sim3** and **Sim4** : *T*=10 s, *A*=2.10^{-2} m such as U_{max}/c_1=1.5 and U_{max}/c_2=5.7 . So this regime is still nonlinear: ε=0.03 and we can additionally expect a hydraulic control of the first and second vertical mode as for **Sim4**. However, in this case, all topographic selection criterions are inferior to one, indicating no selection of vertical modes (table 4). Figure 12-a represent the displacement, in space and time, of the isopycnal line ρ=1044 kg.m^{-3} located at the top of the pycnocline. The strait is located at $\boldsymbol{x_0}$ =1.54 m. Black and white bold contour lines correspond to a mode 1-froude number of one and minus one. There is a mode 1 hydraulic control, $max\ (F_{n,H}{}_{x0}) > \mathbf{1}$. Figure 12-c indicates time evolution of fluid velocity at the shallowest strait depth and dashed lines represent two values of mode 1 celerity: $c_{1,H}$ and $c_{1,D}$ which is mode 1 celerity interpolated at the shallowest strait depth so for a total depth of D (*h*=*D*=0.05m).

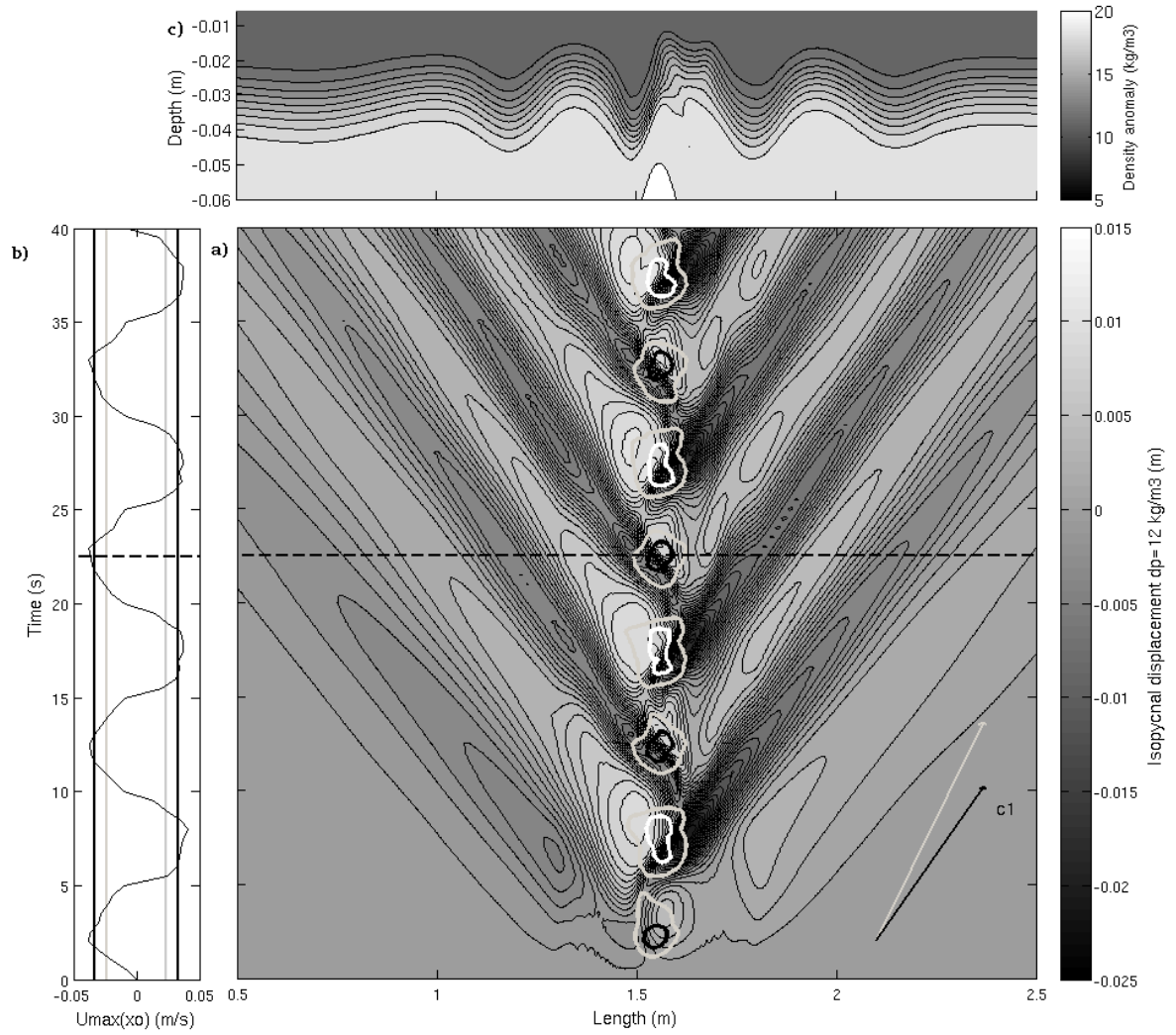

*FIGURE 12 – a) Space-time diagram of the vertical isopycnal displacement for δ ρ=12 kg/m^3(located at the top of the pycnocline) in **Sim5**. Arrows indicate the speed of the first normal mode calculated with modal decomposition method in shallow and deep water ($c_{1,H}$= 0.033 m/s, $c_{1,D}$= 0.023 m/s). White and black contour lines locate mode 1 deep water Froude number of minus one and one. Grey contour lines locate mode 1 shallow water Froude number of an absolute value of one. Horizontal bold dashed line locates temporally the vertical section of the pycnocline.*
b) Temporal evolution of the fluid maximum velocity located just above the ridge (at x_0); vertical lines: (plain bold) $c_{1,H}$, (plain gray) $c_{1,D}$, horizontal bold dashed line locates temporally the vertical section of the pycnocline.
c) Vertical section of the pycnocline at t=22.5s (supercritical flow condition regarding the mode 1 celerity in shallow and deep water)

Only one kind of internal wave propagates along this isopycnal surface, generated during slack tide periods. They correspond to mode 1 structure and celerity and propagate away from the strait. Inspite of the fluid supercriticality and the non-linearity condition, this mode 1 does not degenerate in trains of solitary waves. This is consistent with some numerical and experimental experiments of Dossmann et al.[9]. The authors demonstrate a topographic control mechanism for primary internal solitary wave generation: to generate effectively a topographically induced internal solitary wave in a pycnocline, its wavelength λ and the ridge bottom width, λ_r, must have the same order of

magnitude: $\frac{\lambda}{\lambda_r} \approx 1$. This is also consistent with the condition of maximal mode 1 amplitude indicated by the topographic selection criteria. In this supercritical case, $\frac{\lambda_1}{\lambda_r} = 0.7 < 1$, the amplitude of the first mode is not optimal, the propagation of the mode 1 is quasi-linear and it does not degenerate in trains of solitary waves.

At each tidal reversal, the hydraulic jump is released and propagates above the strait. The wave crest associated to the hydraulic jump becomes steeper and results in a strong inclination of the isopycnal surface but does not seem to break as in **Sim4**. Indeed, the local buoyancy frequency stays positive with the steepening of the hydraulic jump. Figure 12-b shows this phenomenon: during the last tidal period a hydraulic jump was formed on the lee side of the strait, it is then released and induces the propagation of a bore leftward above the strait. The bore steepens and then returns to its original form to continue its way on the other side. Yet, at this point, the kinematic instability condition is reached, the background upstream flow speed is superior to the mode 1 celerity propagating upslope ($u>c_1$) but the shear horizontal current is weaker than in **Sim4**. This can be linked to the amplitude of the first mode and the energy injected into it. The amplitude of the hydraulic jump is smaller as well as the horizontal velocity shear associated to it, so it is more stable and does not break above the strait despite the kinematic instability condition.

To conclude, in this supercritical regime, modes 1 are submitted to hydraulic control but do not disintegrate in periodic trains of ISWs. Thus, they travel smaller distance, impacting the localization of induced remote mixing. Moreover, inspite of the favorable kinematic instability condition, the hydraulic jump does not break above the strait. However, other processes of turbulence cascade, due to the strong tidal forcing and the resulting friction, induce strong local mixing above the strait in the bottom layer. The induced mixing is then localized closer to the bottom than in the previous breaking regime in which IW breaking induces strong diapycnal mixing in the pycnocline.

5.4. A mode 1 hydraulic control with quasi-steady lee waves

Finally, a simulation (**Sim6**), with quasi-steady lee waves is shown in figure 13. The flow is supercritical and trapped internal waves are generated in the lee-side of the strait. Only the amplitude of the tidal forcing varies from **Sim1**: A =0.3 m such as U_{max}/c_1=1.3. This regime is highly nonlinear: ε=0.21 and the mode 1 is subject to hydraulic control. Moreover, the mode 1 topographic selection criteria is superior to one (table 4). In this simulation, the strait top is farther from the pycnocline than in the three previous cases, so the topographic blocking degree is smaller (B=0.7). Figure 13 (right) represents the vertical velocity field and the isopycnal lines of **Sim6** at t=1 min. The vertical stratification profile, the topography and the tidal period of **Sim6** are the same than **Sim1**, however the vertical velocity field of these two simulations are quite different (figure 5-e). Indeed, in **Sim6**, only the first vertical mode is generated (only one maximal velocity value on the vertical and isopycnal lines in phase), whereas in **Sim1**, the four first vertical modes have significant amplitudes (ray pattern i.e. 2.ii) even if in these two configurations the topographic selection criteria are exactly the same. Another difference is the wavelength associated to this first vertical mode. In **Sim1**, the

mode 1 wavelength is very close to the linear analytical value (λ_1=2.2 m- Figure 5). However, in **Sim6**, mode 1 vertical structure is associated to several wavelength (0.49m-0.66m-1m, λ-λ'- λ'' on figure 13), all smaller than the linear analytical value. In both configurations, mode 1 wave celerities are very close to mode 1 linear analytical value (c_1=0.1376 m/s) no matter what the value of the wavelength is. In **Sim6**, the mode 1 small wavelength waves are generated during the hydraulic control period during which they are trapped in the lee-side of the strait.

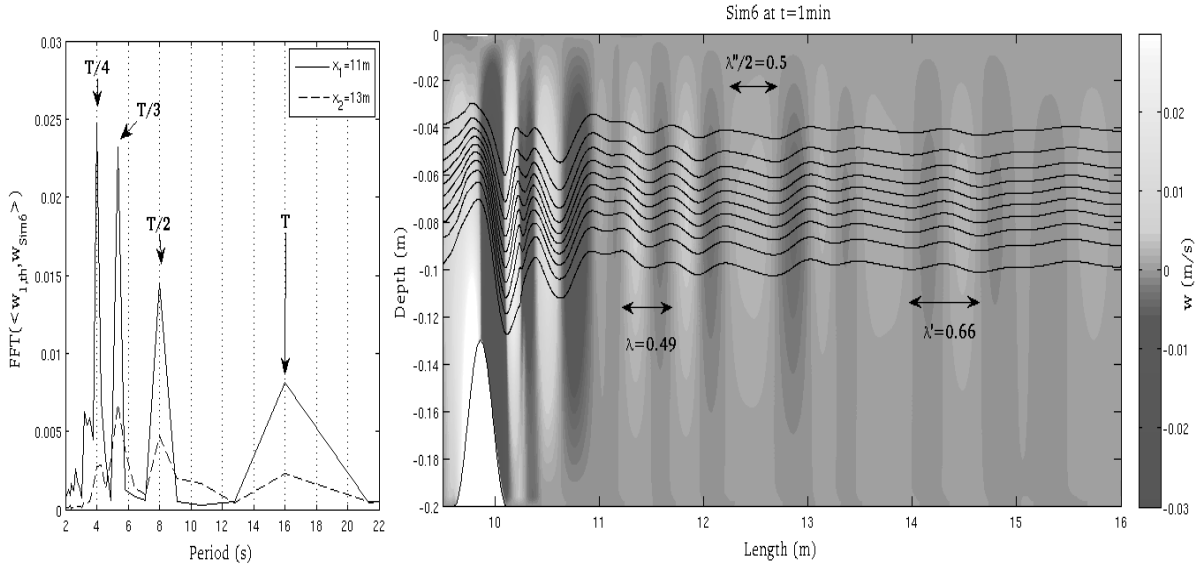

*FIGURE 13 – (Right) Vertical velocity field in **Sim6** at t=1min, contours indicate isopycnal lines, the density difference between two lines is dρ=6 kg.m^{-3} . (Left)FFT of the result of the orthogonal projection of the first analytical vertical mode profile onto the vertical velocity field in **Sim6** at x_1=11 m (plain line) and x_2=13 m(dashed line) for 0-60 second period.*

St Laurent and Garett[44] use the terms "quasi-steady lee wave" to describe the regime illustrated in figure 13. The regime is distinguished using the tidal excursion parameter, A/λ_r, which compares the length of the tidal excursion, A, to the horizontal scale of the topography, λ_r. In the "internal tide" regime, the tidal excursion is less than the scale of the bathymetry and the waves radiate mainly at the fundamental frequency of the tide in both up- and down-stream directions. In the "quasi-steady lee wave" regime, the tidal excursion exceeds the length scale of the bathymetry and waves propagate only in the upstream direction with frequencies < $U(t)/\lambda_r$ and phase speeds < $U(t)$. Higher harmonic internal tides manifest themselves mainly as quasi-steady lee waves.

In **Sim6**, A/λ_r =0.6 which is close to one but is not sufficient to classify this regime as "quasi-steady lee wave" according to St Laurent and Garett[44] and $c_1 < U_{max}$. In order to classify, more precisely this regime, the predominant frequency associated to the mode 1 waves is determined by a Fast Fourier Transform (FFT). First, the mode 1 analytical vertical profile calculated with the modal decomposition method is projected on the vertical velocity profile of **Sim6** at x_1=11m and x_2=13m for the time period t Є [0 60] s. Figure 13 (left) represents the FFT of this scalar product at x_1=11m (plain line) and x_2=13m (dashed line). Near the generation area, the frequency spectrum shows four dominant frequencies: the tidal fundamental frequency (T=16s) and three higher tidal harmonic

frequency ($T/2$= 8s, $T/3$= 5.33s,$T/4$= 4s). When considering a constant mode 1 celerity (c_1=0.1376 m/s), these frequencies correspond to wavelength of 2.2, 1.1, 0.73 and 0.55 m. Moreover, figure 13 shows wavelength of similar order (λ-λ'- λ'') except for the largest one (2.2m) corresponding to the tidal fundamental frequency. For **Sim6**, $U(t)/\lambda_r \in$ [-0.4 0.4] s^{-1} so the condition TLee waves > $\lambda_r /U(t)$ > 2.5 s is respected on the frequency spectrum. The most important frequencies correspond to $T/3$ and $T/4$, so in this regime, the fundamental tidal frequency, T, is no more predominant but higher tidal harmonic are, thus characterizing a "quasi-steady lee wave" regime. Farther from the strait (dashed line on figure 13), higher harmonic frequencies are less important (particularly $T/4$) due to the faster dissipation of smaller wavelength waves. We can notice that the dominant frequencies correspond to wavelength of 0.55-0.73 m roughly matching the width of the strait (λ_r=0.5m). So the topographic selection criteria ($\lambda/\lambda_r \approx 1$) for vertical mode can also be applied for "quasi-steady lee wave", indicating a high amplitude wave response. Similar resonant effect has been observed for atmospheric lee waves (Grubišić and Stiperski[45]).

To conclude, for supercritical flow, when the amplitude of the tidal oscillation (A) becomes approximately of the same order than the strait width, λr, trapped waves are generated in the lee-side of the strait. They have smaller wavelength, so they are more dispersive. These "quasi-steady lee waves" can also break and induce diapycnal local mixing. In such regime, the rate of remote dissipation should be considerably smaller. The topographic blocking parameter, B, seems also to have an influence on this dynamics. Indeed, other numerical simulations (not shown here) suggest that larger topographic blocking parameter ($B \sim 0.9$) in the same supercritical flow condition, even in case of large tidal excursion, seems rather leading to wave breaking above the strait (large eddy). Similar behavior has been observed for atmospheric lee waves. Vosper[46] and Knigge et al.[47] (Figure 9[47]) show that an elevated inversion closed to the top of the mountain is supporting the formation of rotors in the lee side of mountains rather than a lee wave regime.

6. Impact on local circulation : downstream jet formation

All these different internal wave dynamics have an impact on the local circulation in the strait area. Indeed, several studies show an intrinsic connection between hydraulic control of stratified flows and bifurcating streamlines above topographic obstacle (Winters and Armi[48], Baines[49]). Most of them focus on continuously stratified flows or homogenous flow (Smith et al[50]). In particular, Baines[49] studies stratified flow over two dimensional obstacles and highlight three different types of "lee-side" behavior, as a function of the lee-side slope (h_0/l) and NH/U. Different kinds of jets can be generated on the lee-side of the strait. For example, a lee-side bluff body boundary-layer separation results in a jet separation whereas if there is no boundary layer separation on obstacle, a downslope jet can be formed. The next section focuses on the local circulation, in particular the formation of downstream jets, in highly supercritical flow (F_1>>1-table 5-) above supercritical topography in the case of an oscillating flow and an inhomogeneous vertical stratification. These regimes are highly non-linear (ε>>0.018-table 5-).

		Supercritical Fluid F_1>1		
		Jet separation		Downslope jet
		along the slope	at the crest	
		Sim4	**Sim7**	**Sim8**
Initial conditions	A	0.033	0.2	
	λ_r	0.5		1.5
Circulation regime parameters	h_0/l	0.6		0.2
	θ_{th}/γ	0.25		0.68
	A/λ_r	0.066	0.4	0.13
	$Re = \frac{U_0\lambda_r}{\nu}$	2160	13090	39270
	ε	0.05	0.3	0.1
	λ_1/λ_r	1.9		0.6
	$\frac{u_{max}}{c_{1_{th,H}}}$	0.9	5.2	
	$\frac{\delta\rho N_\rho}{U_{max}}$	1.14	0.19	
	$\frac{h_2 N_B}{U_{max}}$	5.10^{-3}	8.10^{-4}	

TABLE 5–Numerical and physical parameters for boundary layer separation regime

6.1. Lee-side vortexes formation and downstream jet separation

A simulation (**Sim7**), with supercritical topography and highly supercritical flow is shown in figure 14-(b) at *t*=34.5 seconds. Only the intensity of the tidal forcing (*A*=0.2 m) varies from **Sim4** (table 5) as the tidal current velocity is multiplied by six. So this regime is highly nonlinear (ε=0.3) and highly supercritical (U_{max}/c_1= 5.2). A comparison is made, at the same time *t*, with the circulation of **Sim4** (figure 14-(a)). In both simulations, flow is supercritical (table 5).

In **Sim4**, at *t*=34.5s (Fig. 14-(a)), the flow is subcritical upstream of the sill and the bottom layer is supercritical just downstream of the crest ($u>c_{1,D}$=0.025 m/s). The bottom layer is accelerated over the obstacle crest forming a downslope jet which start to separate from the topography at *z*=-0.06m. The accelerated layer is asymmetric and thins as it flows past the strait crest. A vortex is created, above the strait crest (*x*≈-0.05m,) at the base of the strongly stratified pycnocline layer (*z*≈-0.035m). It is characterized by shear instability and result in a partially mixed fluid region. This vortex is associated with the beginning of a breaking event (as the one in Figure 11-c) even if, at *t*=34.5 s, the kinematic instability condition has not yet been reached. The separation of the downslope jet is associated to the formation of a small eddy resulting in boundary layer separation. So another vortex is generated inside the bottom layer, in the lee-side of the strait. These two vortexes are associated to two different layers with very different stratification.

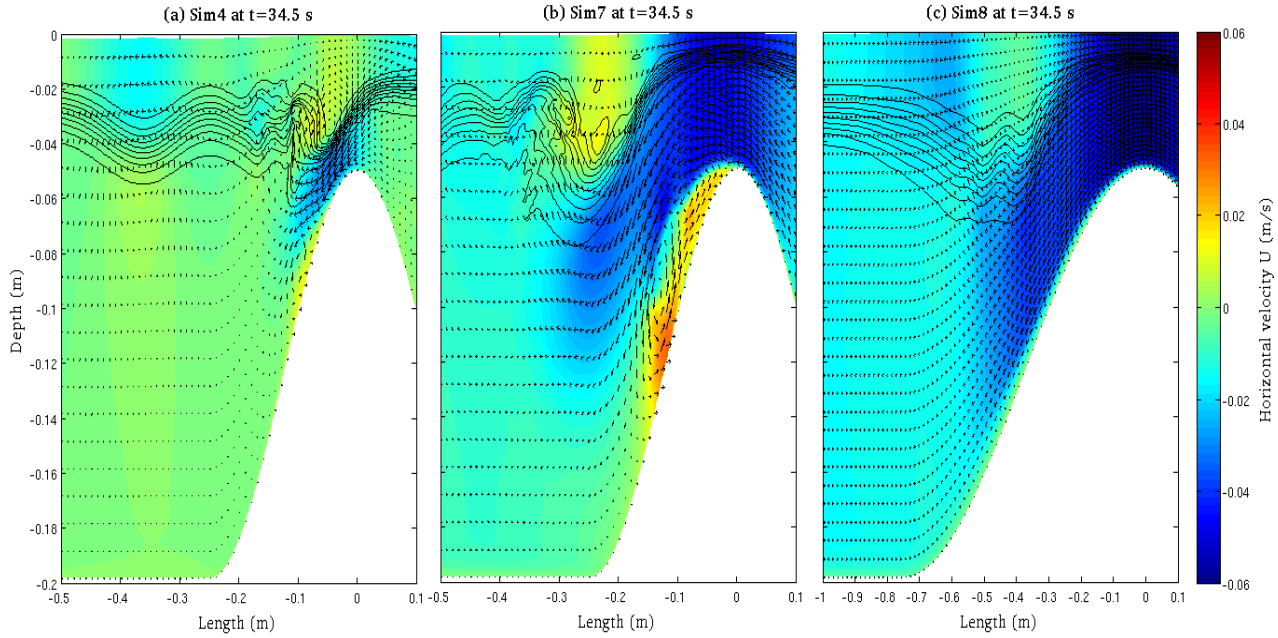

*FIGURE 14 – Vertical section of the strait for three different simulations, at t=34.5 s. The tidal flow is leftward. Color bar represents horizontal velocity output highlighting hydraulic control regions ($u<c_{1,D}$=-0.025m/s). Contour lines represent isopycnal lines, the density difference between two lines is $d\rho$=0.8 kg/m^{-3}. Arrows represent the intensity and the direction of the currents. a)**Sim4** ; b)**Sim7** ; c) **Sim8***

We adapt Baines' criteria for steady and continuously stratified flow at each of these layers and for our oscillating fluid. In the pycnocline layer, the mean stratification N_ρ and the pycnocline thickness, $\delta\rho$, is used: $\frac{\delta\rho N_\rho}{U_{max}} = 1.14$. In the bottom layer, the stratification N_B is very weak: $\frac{h_2 N_B}{U_{max}} = 0.005$. The topography is characterized by a mean slope, h_0/l, of 0.6 (table 5). In this regime, the breaking event in the pycnocline layer and the jet flow separation in the bottom layer correspond to lee-side bluff boundary-layer separation behavior describe by Baines (Fig 5.8, p237 [49]).

In **Sim7**, at *t*=34.5s (Fig. 14-(b)), the flow is supercritical upstream and downstream of the strait ($u>c_{1,D}$=0.025 m/s). The supercritical flow area is much more extended than in **Sim4**. Moreover, above the strait, the flow is nearly barotropic. As the flow pasts the strait crest, this jet separates from the topography slope (*z*=-0.05m). A vortex is created, downstream of the strait (*x*≈-0.25m) at the base of the strongly stratified pycnocline layer (*z*≈-0.04m). Indeed, overturning is visible in the pycnocline layer at *x*=-0.3m, the Brunt-Väisälä Frequency becomes locally negative. This vortex is much larger than the one created in **Sim4** and it is located further downstream due to the more extended and stronger supercritical region. It exerts an opposing force on the fluid, so the jet flow is accelerated and forced by this strong gradient pressure, downward in the bottom layer. Behind this breaking event (at *x*=-0.4), higher modes are locally generated inside the pycnocline. The second vortex created in the bottom layer (*x*=-0.15), associated to the separation of the jet flow from the topography, is also much larger than in **Sim4**. So the separation point moves up the lee slope and the jet start to separate as soon as the flow pasts the strait crest. The pycnocline layer and the bottom

layer also correspond to lee-side bluff boundary-layer separation behavior in this configuration. The Reynolds number is higher ($Re_{Sim7}=13090$) ; this regime is more turbulent than **Sim4** regime with bigger vortex and stronger jet but the dynamic is similar. Both of these regimes can be associated to "high drag state" as the typical response observed near the sill crest during the Knight Inlet Experiment (Farmer and Armi [51]) or can be compared to "downslope windstorm" or mountain-induce rotors (Knigge *et al.*[47]) in analogy to similar phenomena observed with airflow over mountains.

6.2. Downslope jet

A last simulation (**Sim8**) is carried out with a larger strait (λ_r=1.5m), shown in figure 14-(c) at t=34.5 seconds. The topography slope is smoother (h_0/l= 0.2) but still supercritical and all others initial conditions are the same than in **Sim7**. In this configuration, like in Sim7, the hydraulic control area is widespread above the strait (upstream and downstream). The flow is accelerated over the strait then a downslope jet is formed. Contrary to Sim7, the hydraulic jump did not break downstream of the strait but a separation of the flow still occurs beneath this hydraulic jump, this is termed "post-wave" separation. The hydraulic jump forms an adverse pressure gradient creating a stagnant uniform-density isolating region which exerts an opposing force on the fluid. This almost stagnant region, above the pycnocline, isolates the accelerated layer and forced the jet flow downward in the bottom layer. But in this case, the slope is smoother and not in favor of instabilities formation. So, there is no formation of small scale eddies in the lee side of the strait, and there is no separation of the jet flow from the obstacle.

The effect of the slope topography is the same as in Baines' diagram. If the non-dimensional parameter *NH/U* is large enough (as for the pycnocline layer), a steep slope indicates a lee-side bluff body boundary-layer separation whereas a smooth slope correspond to a post wave separation. For a small value of *NH/U* (as for the bottom layer), a steep slope indicates also a lee-side bluff body boundary-layer separation whereas a smooth slope corresponds to no separation on obstacle. Studies on homogeneous flow (Smith et al.[50]) have also shown the importance of the topography slope on boundary separation layer, particularly at high Reynolds number.

To conclude, eddies above and in the lee of the strait may be created if the flow speed is sufficiently large (large F_1), the topography sufficiently steep (large h_0/l) and close to the pycnocline (large B). These eddies have an impact on the local circulation inducing the formation of a downstream jet separated from the topography. Moreover these eddies could have an impact on the turbulent cascade and on the amount of energy dissipated locally.

7. Discussions-conclusions

In straits regions, large topographic variations and strong currents lead to more complex ISWs generation mechanisms and ISWs interactions with their environment. Many different strait configurations and dynamics have been observed and studied in the ocean: hydraulic control with generation of large amplitude mode-1 ISWs (Strait of Gibraltar), internal wave ray impinging on the pycnocline responsible for secondary generation of ISWs (Luzon Strait) but also other kinds of secondary processes due to environmental interaction: advection of a second vertical mode ISW by a first mode ISW (Mascarene ridge), Kelvin-Helmholtz billows in internal wave propagating across a varying topography (Oregon coast)... To provide a better understanding of all these different regimes and processes, an idealized modeling approach has been chosen. Direct numerical simulations of strait dynamics have been presented and a regime analysis has been proposed using and identifying key non-dimensional parameters for ISW dynamics and local circulation associated.

Several statistical and technical tools have been used to analyze these regimes. The orthogonal projection has proved to be an effective method to quantify the amplitude of each vertical mode in linear regime. In non-linear regime, the orthogonal projection as much as the SVD analysis are less effective to quantify the amplitude of vertical modes because vertical modes functions are no more strictly independent. Nevertheless, the SVD analysis permits to highlight the non-linearity character of the regime. The frequency spectrum made from the orthogonal projection is also a good indicator of the non-linear character of the flow. The dominant frequencies indicate three different behaviors:

- Linear internal waves are characterized by a dominant frequency corresponding to the fundamental tidal frequency

- The apparition of higher tidal harmonic frequencies in addition to the dominant fundamental tidal frequency corresponds to non-linear processes in particular internal solitary wave formation (Mercier et al.[52] & Dossmann et al.[53])

- A dominance of higher tidal harmonic frequencies over the fundamental is an indicator of a "quasi-steady lee wave" regime.

Linear regimes have been simulated to study the topographic control on vertical mode generation at supercritical sites. As for small subcritical bottom topography, it is characterized by the ratio of vertical mode wavelength, λ_n, to topography width, λ_r. The amplitudes of the higher modes are larger than at subcritical sites and can exceed the amplitudes of the lowest modes. Indeed energy spreads more homogenously between vertical modes and the topography width selects the maximal modal amplitude (a_n maximal for $\frac{\lambda_n}{\lambda_r} \approx 1$).

In non-linear regime, hydraulic control of higher modes have been simulated and characterized by adapted Froude numbers, F_n, accompanied by the formation of higher mode ISWs. Higher mode ISWs are generated in supercritical straits, if an important part of the energy is injected in this mode

n (implying a topographic selection criterion of $\frac{\lambda_n}{\lambda_r} \approx 1$) and if the non linearity parameter ε, is superior to 0.018 (threshold of Dossmann *et al.*[9]). Moreover, higher mode ISWs propagation distance is highly sensitive to multiple processes of interaction with the environment, as advection by another ISW, topography change and background currents. As a consequence, in some regimes, higher modes ISWs have a very short life and they are blocked above the strait. In other regimes, they can propagate away from the strait. Thus, they can be both actor of remote or local mixing according to the hydraulic and topographic selectivity. Thus, at supercritical sites, not only the well known first mode internal waves but also higher mode baroclinic disturbances should be taken into account in a general balance of mixing processes. Shroyer et al.[54] showed that, although mode-2 waves had for instance less energy than mode-1 waves observed on the coast of New Jersey, the magnitudes of the wave-localized turbulent dissipation were similar in both cases. This suggests that mode-2 internal solitary waves may have a significant effect on eroding the pycnocline and hence on the vertical fluxes of heat and nutrients in the water column. That's why understanding their conditions of disintegration or dissipation could be very useful for vertical mixing parameterizations.

In supercritical flow regime ($F_{1,D} \geq 1$), wave breaking events have also been observed above the strait, characterized by steep slope ratios (highly supercritical topography: $\theta_{th}/\gamma \leq 0.25$, $\frac{\lambda_1}{\lambda_r} \geq 1$). Hydraulic jump breaks above the strait and leads to strong local mixing. This breaking event is due to a mixed of kinematic instability and Kelvin-Helmholtz instability.

A quasi-steady lee waves regime has also been characterized for supercritical flow ($F_{1,D} \geq 1$) and large tidal excursion, A. This regime leads to the generation of smaller wavelength internal waves, so to most dissipative waves. In such situations, the proportion of remote dissipation should be significantly smaller. The dominant wavelengths of these quasi-lee waves are also submitted to a topographic control. Thus, the topographic selection criterion is also, here, a good indicator of the dominant wavelength.

Finally, in some highly turbulent regimes, small scale eddies, above and in the lee of the strait, have been simulated. These eddies are created if the flow speed is sufficiently high (supercritical flow) and the topography sufficiently steep (highly supercritical topography, $\theta_{th}/\gamma \leq 0.25$). They induce the formation of a downstream jet separated from the topography. The formation of such eddies may increase the rate of the local dissipation.

A striking point is the difficulty to establish key non-dimensional parameters which take into account the spatial and the temporal variability of the dynamics. The topographic selection criterion, $\frac{\lambda_n}{\lambda_r}$, has proven to be a useful indicator for the energy distribution between vertical modes even in the case of large topography and supercritical tidal flow. Consequently, it is also a good indicator for solitary wave's generation and for wave overturning occurrence. For the non-linearity parameter, ε, the same solitary wave threshold ($\varepsilon \geq 0.018$) as Dossmann[9] has been found. However, this threshold may shift for higher vertical mode. The "shallow water" Froude number, $F_{n,D}$, has

proven to be accurate and robust to characterize hydraulic control state above the strait. Supercritical flows above varying topography impact vertical modes amplitudes. Thus, the Froude number is also an indicator of hydraulic selectivity of vertical modes and breaking event occurrence. When the tidal excursion is approximately large compared to topography width, this parameter is an indicator of a quasi-pseudo lee-wave regime. The influence of the topographic blocking degree remains to be further examined.

In conclusion, all of these numerical simulations demonstrate that internal waves dynamics, at supercritical sites, are highly diversified and deeply affected by the environment (topography geometry, tidal current, incoming waves). All these environmental factors are related in a non-linear way and must be considered in a global context. Moreover, in the ocean, they are many others interrelated factors that can play a role in the internal waves dynamics, including spatially varying stratification, Coriolis force or more complex topography... The purpose of the Part II is to extend the present study towards more realistic oceanic conditions. In this regard, the present regime analysis is applied to idealized large scale oceanic cases and to two well-known realistic cases: the Strait of Gibraltar and Georges Bank.

8. Appendix

Appendix 1 : Modal decomposition

The principle of modal decomposition (Gill[55]) rests on the rigid-lid approximation justified by weak free-surface displacements. It applies to any buoyancy profile N(z), and to flat bottom condition. Linear solutions of the Boussinesq equation for the vertical velocity field, w, are seeked in the form:

$$w(x,z,t) = W_n(z)e^{i(k_n x-\omega t)}$$

where W_n, k_n, are respectively the vertical modal structure and the wavenumber, ω is the wave pulsation and $n \in N^*$ is the mode number. W_n et k_n are solutions of the Sturm-Liouville eigenvalue problem:

$$\frac{\partial^2 W_n(z)}{\partial z^2} + {k_{x,n}}^2\left(\frac{N^2(z)-\omega^2}{\omega^2}\right)W_n(z) = 0$$

$$W_n(0) = 0 \text{ et } W_n(-H) = 0$$

Appendix 2 : Singular value decomposition (SVD)

Singular value decomposition (SVD) analysis on vertical velocity field is used to determine which vertical modes are dominant. The Singular value decomposition (SVD) analysis is a decomposition of the vertical velocity data set ($w(z,t)$) in terms of orthogonal basis functions which are determined from the data. The SVD method finds both time series and vertical spatial patterns associated to these empirical orthogonal functions (EOF). Note that vertical modes are orthogonal function under

flat bottom conditions. The singular value decomposition of the $z \times t$ matrix W is a factorization of the form $W = U\Sigma V*$, where U is $z \times k$ with orthonormal columns, Σ is $k \times k$ rectangular diagonal with non-negative real numbers on the diagonal, and $V*$ is $k \times t$ with orthonormal columns. We compute the four largest singular values (k=4) and associated singular vectors of matrix W. The singular vectors U and V represent respectively time series and spatial patterns associated to EOFs.

Appendix 3: Orthogonal projection

To determine each vertical mode amplitude (A_n) in our simulations, an orthogonal projection analysis on vertical velocity field is used. Vertical modal structures ($W_n(z)$), calculated with the modal decomposition method, are projected on the vertical velocity field ($w(x,z,t)$). For each resulting projection ($P_{n,w}(x,t)$), we calculate the residual signal ($w(x,z,t) - \sum_{i=1}^{n-1} P_{i,w}(x,t).W_i(z)$) before applying the next vertical mode projection :

$$P_{n,w}(x,t) = \langle w(x,z,t) - \sum_{i=1}^{n-1} P_{i,w}(x,t).W_i(z), W_n(z) \rangle$$

Frequency spectra were calculated on $P_{n,w}(x,t)$ by a fast Fourier transform. In Fourier analysis a signal is decomposed into its constituent sinusoidal vibrations. In our configurations, there is only one tidal frequency but tidal harmonic can be generated. Moreover, non-linearity can induce the emerging of additional characteristic frequencies on the frequency spectra (Mercier et al.[52], Dossmann et al.[30]). In oceanic configurations, there are several tidal forcing frequencies, so filtering is highly necessary. The amplitude of the spectrum at the tidal frequency, $P_{n,w}(x, f_{internal\ tide})$, gives the amplitude of the associated vertical mode ($A_{n,w}(x)$).

9. References

[1] W. Munk and C. Wunsch, "Abyssal Recipes II: Energetics of Tidal and Wind Mixing", Deep Sea Res. Part Oceanogr. Res. Pap., **45**, 1977 (1998).

[2] G.D. Egbert and R.D. Ray, "Significant Dissipation of Tidal Energy in the Deep Ocean Inferred from Satellite Altimeter Data", Nature, **405**, 775 (2000).

[3] C. Wunsch and R. Ferrari, "Vertical Mixing, Energy, and the General Circulation of the Oceans", Annu. Rev. Fluid Mech., **36**, 281 (2004).

[4] A.K. Liu, J.R. Holbrook, and J.R. Apel, "Nonlinear Internal Wave Evolution in the Sulu Sea", J. Phys. Oceanogr., **15**, 1613 (1985).

[5] Y.-J. Yang, T.Y. Tang, M.H. Chang, A.K. Liu, M.-K. Hsu, and S.R. Ramp, "Solitons Northeast of Tung-Sha Island during the ASIAEX Pilot Studies", IEEE J. Ocean. Eng., **29**, 1182 (2004).

[6] T.F. Duda, J.F. Lynch, J.D. Irish, R.C. Beardsley, S.R. Ramp, C.-S. Chiu, T.Y. Tang, and Y.-J. Yang, "Internal Tide and Nonlinear Internal Wave Behavior at the Continental Slope in the Northern South China Sea", IEEE J. Ocean. Eng., **29**, 1105 (2004).

[7] J.M. Klymak, R. Pinkel, C.-T. Liu, A.K. Liu, and L. David, "Prototypical Solitons in the South China Sea", Geophys. Res. Lett., **33**, L11607 (2006).

[8] D.M. Farmer, L. Armi, L. Armi, and D.M. Farmer, "The Flow of Atlantic Water through the Strait of GibraltarThe Flow of Mediterranean Water through the Strait of Gibraltar", Prog. Oceanogr., **21**, 1 (1988).

[9] Y. Dossmann, F. Auclair, and A. Paci, "Topographically Induced Internal Solitary Waves in a Pycnocline: Primary Generation and Topographic Control", Phys. Fluids, **25**, 066601 (2013).
[10] Y. Dossmann, F. Auclair, and A. Paci, "Topographically Induced Internal Solitary Waves in a Pycnocline: Secondary Generation and Selection Criteria", Phys. Fluids, **25**, 086603 (2013).
[11] A.L. New and R.D. Pingree, "Large-Amplitude Internal Soliton Packets in the Central Bay of Biscay", Deep Sea Res. Part Oceanogr. Res. Pap., **37**, 513 (1990).
[12] A.L. New and R.D. Pingree, "Local Generation of Internal Soliton Packets in the Central Bay of Biscay", Deep Sea Res. Part Oceanogr. Res. Pap., **39**, 1521 (1992).
[13] A.L. New and J.C.B. Da Silva, "Remote-Sensing Evidence for the Local Generation of Internal Soliton Packets in the Central Bay of Biscay", Deep Sea Res. Part Oceanogr. Res. Pap., **49**, 915 (2002).
[14] D. Farmer and L. Armi, "The Flow of Atlantic Water Through the Strait of Gibraltar - the Flow of Mediterranean Water Through the Strait of Gibraltar", Prog. Oceanogr., **21**, 1 (1988).
[15] T. Maxworthy, "A Note on the Internal Solitary Waves Produced by Tidal Flow over a Three-Dimensional Ridge", J Geophys Res, **84**, 338 (1979).
[16] V. Vlasenko and W. Alpers, "Generation of Secondary Internal Waves by the Interaction of an Internal Solitary Wave with an Underwater Bank", J. Geophys. Res. Oceans, **110**, C02019 (2005).
[17] V. Vlasenko, N. Stashchuk, and K. Hutter, *Baroclinic Tides: Theoretical Modeling and Observational Evidence* (Cambridge University Press, 2005).
[18] J. Klymak, S. Legg, M. Alford, M. Buijsman, R. Pinkel, and J. Nash, "The Direct Breaking of Internal Waves at Steep Topography", Oceanography, **25**, 150 (2012).
[19] P.F. Cummins, "Stratified Flow over Topography: Time-Dependent Comparisons between Model Solutions and Observations", Dyn. Atmospheres Oceans, **33**, 43 (2000).
[20] C. Jackson, J. da Silva, and G. Jeans, "The Generation of Nonlinear Internal Waves", Oceanography, **25**, 108 (2012).
[21] A. Vázquez, N. Stashchuk, V. Vlasenko, M. Bruno, A. Izquierdo, and P.C. Gallacher, "Evidence of Multimodal Structure of the Baroclinic Tide in the Strait of Gibraltar", Geophys. Res. Lett., **33**, L17605 (2006).
[22] J.C.B. da Silva, A.L. New, and J.M. Magalhaes, "On the Structure and Propagation of Internal Solitary Waves Generated at the Mascarene Plateau in the Indian Ocean", Deep Sea Res. Part Oceanogr. Res. Pap., **58**, 229 (2011).
[23] Y.J. Yang, Y.C. Fang, M.-H. Chang, S.R. Ramp, C.-C. Kao, and T.Y. Tang, "Observations of Second Baroclinic Mode Internal Solitary Waves on the Continental Slope of the Northern South China Sea", J. Geophys. Res. Oceans, **114**, C10003 (2009).
[24] D.M. Farmer and J. Dungan Smith, "Tidal Interaction of Stratified Flow with a Sill in Knight Inlet", Deep Sea Res. Part Oceanogr. Res. Pap., **27**, 239 (1980).
[25] T.R. Akylas, R.H.J. Grimshaw, S.R. Clarke, and A. Tabaei, "Reflecting Tidal Wave Beams and Local Generation of Solitary Waves in the Ocean Thermocline", J. Fluid Mech., **593**, 297 (2007).
[26] T. Gerkema, "Internal and Interfacial Tides: Beam Scattering and Local Generation of Solitary Waves", J. Mar. Res., **59**, 227 (2001).
[27] N. Grisouard, C. Staquet, and T. Gerkema, "Generation of Internal Solitary Waves in a Pycnocline by an Internal Wave Beam: A Numerical Study", J. Fluid Mech., **676**, 491 (2011).
[28] M. Carr, P.A. Davies, and R.P. Hoebers, "Experiments on the Structure and Stability of Mode-2 Internal Solitary-like Waves Propagating on an Offset Pycnocline", Phys. Fluids 1994-Present, **27**, 046602 (2015).
[29] E.L. Shroyer, J.N. Moum, and J.D. Nash, "Mode 2 Waves on the Continental Shelf: Ephemeral Components of the Nonlinear Internal Wavefield", J. Geophys. Res. Oceans, **115**, C07001 (2010).
[30] Y. Dossmann, A. Paci, F. Auclair, M. Lepilliez, and E. Cid, "Topographically Induced Internal Solitary Waves in a Pycnocline: Ultrasonic Probes and Stereo-Correlation Measurements", Phys. Fluids, **26**, 056601 (2014).
[31] F. Auclair, C. Estournel, J.W. Floor, M. Herrmann, C. Nguyen, and P. Marsaleix, "A Non-Hydrostatic Algorithm for Free-Surface Ocean Modelling", Ocean Model., **36**, 49 (2011).

[32] F. Auclair, L. Bordois, Y. Dossmann, T. Duhaut, A. Paci, C. Ulses, and C. Nguyen, "A Non-Hydrostatic Non-Boussinesq Algorithm for Free-Surface Ocean Modelling", Ocean Model., in revision, (First submitted 2014).

[33] F. Auclair, L. Bordois, Y. Dossmann, T. Duhaut, C. Estournel, J.W. Floor, P. Marsaleix, C. Nguyen, A. Paci, and C. Ulses, "Implementation of a Time-Dependent Bathymetry in a Free-Surface Ocean Model: Application to Internal Wave Generation", Ocean Model., **80**, 1 (2014).

[34] T. Gerkema and J.T.F. Zimmerman, "An Introduction to Internal Waves: Lecture Notes", R. NIOZ, (2008).

[35] L. Armi, "The Hydraulics of Two Flowing Layers with Different Densities", J. Fluid Mech., **163**, 27 (1986).

[36] G. Sannino, A. Bargagli, and V. Artale, "Numerical Modeling of the Mean Exchange through the Strait of Gibraltar", J. Geophys. Res. Oceans, **107**, 9 (2002).

[37] K.B. Winters and L. Armi, "Hydraulic Control of Continuously Stratified Flow over an Obstacle", J. Fluid Mech., **700**, 502 (2012).

[38] T. Gerkema and J.T.F. Zimmerman, "An Introduction to Internal Waves", Lect. Notes R. NIOZ Texel, (2008).

[39] Vlasenko,Stashchuk, Hutter, *Baroclinic Tides, Theoretical Modeling and Observational Evidence.* (Cambridge University Press (2005), 2005).

[40] C. Guo, V. Vlasenko, W. Alpers, N. Stashchuk, and X. Chen, "Evidence of Short Internal Waves Trailing Strong Internal Solitary Waves in the Northern South China Sea from Synthetic Aperture Radar Observations", Remote Sens. Environ., **124**, 542 (2012).

[41] V. Vlasenko and N. Stashchuk, "Amplification and Suppression of Internal Waves by Tides over Variable Bottom Topography", J. Phys. Oceanogr., **36**, 1959 (2006).

[42] V. Vlasenko and K. Hutter, "Numerical Experiments on the Breaking of Solitary Internal Wavesover a Slope–Shelf Topography", J. Phys. Oceanogr., **32**, 1779 (2002).

[43] F.-S.P. Timothy W. Kao, "Internal Solitons on the Pycnocline: Generation, Propagation, and Shoaling and Breaking over a Slope", J. Fluid Mech., **159**, 19 (1985).

[44] L. St. Laurent and C. Garrett, "The Role of Internal Tides in Mixing the Deep Ocean", J. Phys. Oceanogr., **32**, 2882 (2002).

[45] V. Grubišić and I. Stiperski, "Lee-Wave Resonances over Double Bell-Shaped Obstacles", J. Atmospheric Sci., **66**, 1205 (2009).

[46] S.B. Vosper, "Inversion Effects on Mountain Lee Waves", Q. J. R. Meteorol. Soc., **130**, 1723 (2004).

[47] C. Knigge, D. Etling, A. Paci, and O. Eiff, "Laboratory Experiments on Mountain-Induced Rotors", Q. J. R. Meteorol. Soc., **136**, 442 (2010).

[48] Winters, "Topographic Control of Stratified Flows: Upstream Jets, Blocking and Isolating Layers", J. Fluid Mech., **753**, 80 (2014).

[49] P.G. Baines, *Topographic Effects in Stratified Flows* (Cambridge University Press, 1998).

[50] F.T. Smith, P.W.M. Brighton, P.S. Jackson, and J.C.R. Hunt, "On Boundary-Layer Flow Past Two-Dimensional Obstacles", J. Fluid Mech., **113**, 123 (1981).

[51] D.M. Farmer and L. Armi, "The Generation and Trapping of Solitary Waves over Topography", Science, **283**, 188 (1999).

[52] M.J. Mercier, L. Gostiaux, K. Helfrich, J. Sommeria, S. Viboud, H. Didelle, S.J. Ghaemsaidi, T. Dauxois, and T. Peacock, "Large-Scale, Realistic Laboratory Modeling of M2 Internal Tide Generation at the Luzon Strait", Geophys. Res. Lett., **40**, 5704 (2013).

[53] Y. Dossmann, A. Paci, F. Auclair, M. Lepilliez, and E. Cid, "Topographically Induced Internal Solitary Waves in a Pycnocline: Ultrasonic Probes and Stereo-Correlation Measurements", Phys. Fluids 1994-Present, **26**, 056601 (2014).

[54] E.L. Shroyer, J.N. Moum, and J.D. Nash, "Mode 2 Waves on the Continental Shelf: Ephemeral Components of the Nonlinear Internal Wavefield", J. Geophys. Res. Oceans, **115**, C07001 (2010).

[55] A.E. Gill, *Atmosphere-Ocean Dynamics* (Academic Press, 1982).

10.**Compléments**

Nous avons montré, précédemment, que le résultat des projections orthogonales des modes verticaux sur le champ de vitesse verticale w, à l'aide d'une analyse de Fourier, permettait de caractériser les régimes de « pseudo-ondes de sillage » tels qu'observés dans l'expérience **Sim6** (section 5.4). Rappelons que les régimes de « pseudo-ondes de sillage », par définition, présentent des fréquences d'oscillations caractéristiques différentes de la fréquence fondamentale de la marée. Mercier et al. (2013) et Dossmann et al. (2014) ont montré que des processus non-linéaires tels que les ondes internes solitaires pouvaient induire l'émergence de fréquences caractéristiques additionnelles sur le spectre de fréquence. Ils ont, en particulier, utilisé une technique de transformée de Fourier pour caractériser la génération secondaire d'ondes internes solitaires. Dans de telles conditions, Mercier et al. (2013), montrent que le spectre en fréquence présente un bombement à haute fréquence. Notre approche est un peu différente puisque la projection orthogonale est utilisée dans un premier temps pour isoler le signal d'un mode vertical de la façon décrite dans l'annexe 2. On peut donc se demander de quelle façon les ondes internes solitaires vont être caractérisées en termes de spectre de fréquence en utilisant notre approche. Dans la continuité de cet article, nous nous intéressons à des cas de générations primaires.

La Figure 3.1 montre une application de cette approche sur trois simulations différentes : **Sim1**, **Sim9** et **Sim6**. Les mêmes conditions initiales sont utilisées dans ces trois simulations (**Sim1**-tableau 3) excepté pour l'amplitude d'oscillation de la topographie A. De ce fait, les profils théoriques des modes verticaux calculés par la méthode de décomposition modale sont identiques pour les trois simulations. Le critère de sélection topographique est également identique (λ_1/λ_r = 4.4). Pour une comparaison optimale on utilise toujours la même fenêtre temporelle t ∈ $[80s\ 110s]$ pour effectuer la transformée de Fourier. Le forçage augmente en amplitude dans ces trois simulations : A= [6.10^{-3} ; 0.06 ; 0.3] m. De ce fait, l'expérience **Sim1** correspond à un régime linéaire (section 4.2) alors que **Sim9** correspond à un régime non-linéaire (ε = 0.042 > 0.018), sans contrôle hydraulique ($F_{1,D} = 0.33 < 1$), avec formation d'onde internes solitaires de mode 1 ($\lambda_1/\lambda_r \geq 1$). Notons que dans notre configuration, lorsque l'on augmente l'amplitude d'oscillation de la topographie A, on augmente à la fois les courants et l'excursion de la marée. L'expérience **Sim6** caractérise un régime de « pseudo-ondes de sillage » (section 5.4). La Figure 3.1 représente le spectre de fréquence de ces trois différents régimes.

Ces 3 spectres sont caractérisés par des pics de fréquences différents:

- Le spectre en fréquence du régime linéaire (A) présente un seul pic à la fréquence fondamentale de la marée.

- Le régime non-linéaire avec formation d'ondes solitaires (B) présente 4 pics de fréquence, un maximum pour la fréquence fondamentale de la marée et les trois suivants correspondent aux harmoniques supérieures.

- Le spectre de fréquence du régime « pseudo-ondes de sillage » (C) ne présente plus de pic maximal à la fréquence fondamentale de la marée, les trois premières fréquences harmoniques dominent le spectre.

En conclusion, on observe bien l'émergence de fréquences caractéristiques additionnelles sur le spectre de fréquence dans le cas de la génération primaire d'ondes internes solitaires. Dans ce type de régime, la fréquence fondamentale reste cependant dominante. Dans cette situation de génération primaire d'ondes internes solitaires, le spectre de fréquence ne présente pas un bombement à haute fréquence, tel que celui observé par Mercier dans le cas de la génération secondaire.

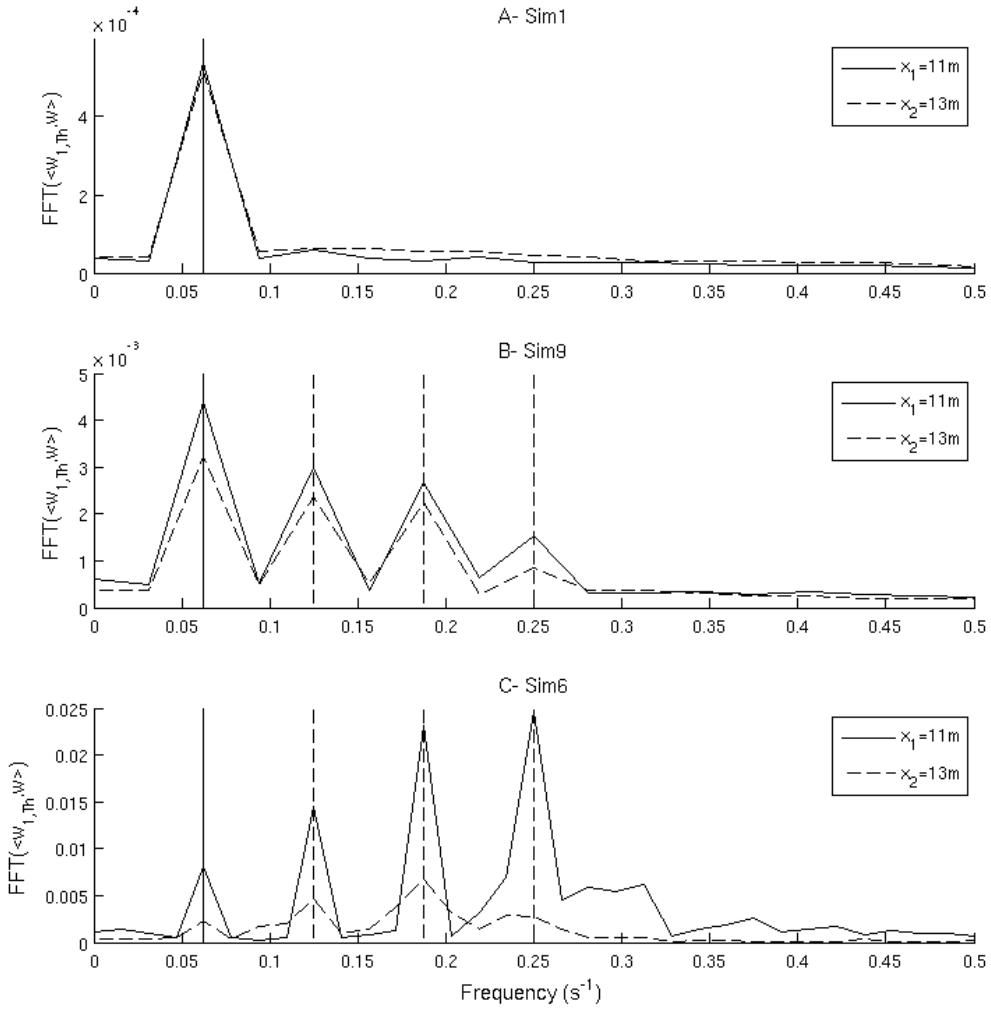

*Figure 3.1 : Transformée de Fourier du produit de la projection orthogonale du profile analytique du mode 1 sur le champ de vitesse verticale des simulations **Sim1** (A), **Sim9** (B), **Sim6** (C) pour une période de 80 à 110 secondes à x_1=11 m (ligne plaine) et x_2=13 m (ligne en pointillé) . La ligne verticale pleine positionne la fréquence fondamentale de la marée et les lignes verticales en pointillé la fréquence des quatres premières harmoniques.*

Dans ce chapitre, des simulations numériques directes ont permis de décrire quantitativement la génération primaire et la dynamique des ondes internes dans la pycnocline sur une large gamme de régimes « supercritiques ». L'influence de la largeur de la topographie sur la génération des modes verticaux d'ondes internes à la fois au-dessus de topographies sous-critiques et supercritiques a été mise en évidence dans nos simulations. Ces régions peuvent notamment être caractérisées par des modes hauts de grande amplitude. Cependant la propagation de ces modes hauts et leur devenir sont très sensibles aux conditions environnementales (topographie, courant barotrope, interactions ondes-ondes …) ce qui rend leur prévision d'autant plus complexe. Ils peuvent notamment être acteurs du mélange local ou se propager au-delà de leur zone de génération. La dynamique des ondes internes dans les régions « supercritiques » est donc très diversifiée et fortement influencée par les conditions environnementales (courants, topographies…). De plus, tous ces facteurs environnementaux sont interconnectés et doivent donc être considérés de façon globale. Il reste, dans l'océan, de nombreux autres facteurs pouvant jouer un rôle dans la dynamique des ondes internes. En ce sens, l'objectif du chapitre suivant est d'étendre cette étude de régime « supercritique » à des conditions océaniques plus réalistes et plus complexes.